Research Square

Preprints are preliminary reports that have not undergone peer review.
They should not be considered conclusive, used to inform clinical practice,
or referenced by the media as validated information.

Bias-corrected upper-ocean data for impact assessments of global warming and assimilation into climate models

Yusuke Ushijima

ushijima.yusuke.fp@ehime-u.ac.jp

Ehime University

Hiroyuki Tsujino

Meteorological Research Institute

Ryo Mizuta

Meteorological Research Institute

Hideyuki Nakano

Meteorological Research Institute

Hirokazu Endo

Meteorological Research Institute

Hideo Shiogama

National Institute for Environmental Studies

Yukiko Imada

The University of Tokyo

Osamu Arakawa

Japan Agency for Marine-Earth Science and Technology

Seiji Yukimoto

Meteorological Research Institute

Yuma Kawakami

Meteorological Research Institute

L. Shogo Urakawa

Meteorological Research Institute

Takahiro Toyoda

Meteorological Research Institute

Masayoshi Ishii

Meteorological Research Institute

---

data-descriptor

Keywords:

Posted Date: October 6th, 2026

DOI: https://doi.org/10.21203/rs.3.rs-10928820/v1

License: This work is licensed under a Creative Commons Attribution 4.0 International License.
Read Full License

Additional Declarations: No competing interests reported.

Bias-corrected upper-ocean data for impact assessments of global warming and assimilation into climate models

Yusuke Ushijima[1], Hiroyuki Tsujino[2], Ryo Mizuta[2], Hideyuki Nakano[2], Hirokazu Endo[2], Hideo Shiogama[3], Yukiko Imada[2,4], Osamu Arakawa[5], Seiji Yukimoto[2], Yuma Kawakami[2], L. Shogo Urakawa[2], Takahiro Toyoda[2], and Masayoshi Ishii[2]

[1]Center for Marine Environmental Studies, PIAS, Ehime University, Matsuyama, Japan
[2]Meteorological Research Institute, Tsukuba, Japan
[3]Earth System Division, National Institute for Environmental Studies, Tsukuba, Japan
[4]Atmosphere and Ocean Research Institute, University of Tokyo, Tokyo, Japan
[5]Japan Agency for Marine-Earth Science and Technology, Yokohama, Japan
[*]Correspondence: ushijima.yusuke.fp@ehime-u.ac.jp

Abstract

We developed monthly time-series datasets of upper-ocean temperature, salinity, and sea-ice concentration for non-warming (NW) and future climate conditions, which are intended to be assimilated into the ocean components of climate models to improve the accuracy of simulations under various climate conditions. Monthly time series of upper-ocean temperature and salinity from an observation-based objective analysis over the past 60 years were decomposed into climatological, externally forced, and internal variability components. The climatological component was defined as the 60-year monthly mean. The externally forced components were extracted using empirical orthogonal function analysis applied to climate model simulations from the Coupled Model Intercomparison Project Phase 6 (CMIP6). Internal variability was estimated as the residual obtained by removing the climatological and externally forced components from the original time series. The NW dataset was constructed by adding the monthly climatology for 1850–1899, which was estimated as the climatology for the past 60 years after removing the externally forced component, to the internal variability component. The NW dataset represents climate conditions with a global-mean sea surface temperature approximately 0.37 °C lower than that of the present climate. Future datasets were constructed consistently with the Shared Socioeconomic Pathway scenarios and include scenario-dependent warming trends and sea-ice declines. This framework corrects climatological biases in CMIP6 simulations while preserving externally forced changes. The resulting dataset, when assimilated into the ocean-sea ice components of climate models, would provide a robust basis for quantifying the impacts of anthropogenic warming in climate model simulations.

Background & Summary

There is a growing demand for more accurate climate projection datasets because datasets for the past, present, and future climate states have recently begun to be used to design adaptation and mitigation strategies in face of global warming. Currently, datasets are primarily based on the outputs of coupled global climate models (CGCMs) and Earth system models (ESMs) participating in the Coupled Model Intercomparison Project (CMIP). However, these models exhibit systematic biases in sea surface temperature (SST)[1,2,3], and the SST biases propagate into the atmospheric component[4,5]. For example, persistent biases in the Intertropical Convergence Zone (ITCZ) and the midlatitude westerly jets, both of which are critical elements of climate projections, are linked to underlying SST biases[6,7]. Previous studies demonstrate that these atmospheric biases can be substantially reduced when more realistic SST is prescribed in atmospheric model simulations[8,9,10]. These findings highlight the importance of reducing climatological SST biases in coupled models when assessing atmospheric circulation responses. This has motivated the development of atmospheric model experiments forced by prescribed SSTs in non-warming (NW) and future climates.

In response to these issues, atmospheric model experiments with prescribed SST and the corresponding sea ice concentration (SIC) that are based on observed climatology have been widely used to assess the impacts of anthropogenic climate change in present climates[11,12,13,14,15] and to project future climate changes[8,16,17]. Based on these approaches, coordinated experimental frameworks for creating datasets of climate states in past, present, and future, such as the Half a degree Additional warming, Prognosis and Projection, and Impact (HAPPI)[18], the High Resolution Model Intercomparison Project (HighResMIP)[19], and the Database for Policy Decision-Making for Future climate change (d4PDF)[20], were developed and are now widely used to assess the impact of global warming. For example, d4PDF has been utilized to assess future river flooding associated with heavy rainfall[21,22], coastal flooding from storm surges[23], and a variety of other environmental and societal impacts[24,25,26], as summarized by Ishii and Mori[27]. In addition, d4PDF includes NW simulations representing pre-industrial conditions, which have been used for attribution studies of extreme events[28,29,30], including heavy precipitation[31,32,33] and high-temperature events[34,35] that are currently occurring.

Future climate impact assessments have often been conducted based on specific global warming levels, such as 1.5 K, 2 K, or 4 K increases in global mean surface air temperature (GMSAT).

This approach is partly justified by the fact that many climate-related phenomena can be approximately scaled with GMSAT[36,37]. However, challenges remain for phenomena affected by multi-year histories of temperature and precipitation, such as water resources and agriculture, as well as for processes like snow accumulation, for which the validity of simple scaling relationships remains uncertain[38]. In addition, there has been increasing demand for information on when anthropogenic signals emerge from natural variability[39], highlighting the need for datasets that represent continuous warming from the present to future climates. Although HighResMIP simulates continuous climate changes, the prescribed SST used in these simulations is estimated from the multi-model mean under a single emission scenario[19]. Because climate projections are substantially affected by both models and emission scenarios[40,41], impact assessments intended to inform policy decision-making require evaluation frameworks that explicitly incorporate uncertainties arising from both models and scenarios. Therefore, there is a need for datasets representing continuous SST changes that take into account model and scenario uncertainties.

Furthermore, when SST is prescribed as in the previous experiments using atmospheric models, interactive air–sea feedbacks cannot be represented, which may lead to biases such as those in tropical cyclones[42]. To overcome these limitations, an approach that assimilates upper-ocean temperature and salinity without imposing overly strong constraints has been proposed to reduce SST biases while preserving coupled atmosphere–ocean processes[5]. As datasets complementary to d4PDF that prescribed SST, new climate simulations for the recent past have been conducted using a climate model based on the Meteorological Research Institute (MRI) ESM version 2.0 (MRI-ESM2-0) with ocean data assimilation[43]. Assimilation of upper-ocean temperature and salinity reduces the atmospheric biases induced by SST biases in CMIP coupled models including ITCZ and westerly jets. Unlike d4PDF, these simulations allow short-term air-sea interactions and successfully capture the latitudinal dependence of intense tropical cyclones. However, the lack of bias-reduced, seamless upper-ocean datasets spanning present and future climate conditions for assimilation has limited the application of these frameworks to future climate projection experiments starting from the present state.

Here, to enable simulations in future climate, as well as in NW climate, using coupled models with ocean data assimilation, we develop monthly upper-ocean temperature, salinity, and SIC time-series for those climate conditions. Our upper-ocean datasets are constructed largely following the methods used in the previous studies to estimate SST and SIC, albeit with some modifications. The upper-ocean temperature and salinity are decomposed into three

components: climatology, externally forced change, and internal variability. The climatological component is defined as the 60-year monthly mean of an observation-based objective analysis. The externally forced components are extracted from climate model simulations from the CMIP Phase 6 (CMIP6) for both past and future. Internal variability is estimated as the residual obtained by removing the climatological and externally forced components from the original time series of the observation-based objective analysis. This approach explicitly accounts for externally forced change in CMIP6 simulations while reducing atmospheric errors in coupled models associated with SST climatological biases, since anomalies from climatology are used to estimate externally forced change.

The externally forced change is extracted through empirical orthogonal function (EOF) analysis of the ensemble-mean SSTs from CMIP6 coupled models and represented as a combination of the resulting forced modes. The forced modes are identified based on their explained variance and the signal-to-noise (S/N) ratios. EOF analysis shows that externally forced SST change is well represented by the first EOF mode across all models. However, since a second EOF mode also contributes non-negligibly in some scenarios and models and has sufficiently large S/N ratios, it is treated as an externally forced mode in many models. The extracted forced modes are projected onto interior temperature and salinity to construct three-dimensional data. The resulting externally forced changes are then used to generate the NW and future datasets. The NW dataset represents pre-industrial conditions, with a global-mean SST (GMSST) approximately 0.37 °C lower than that of the past 60 years. Future datasets are constructed consistently with the Shared Socioeconomic Pathway (SSP) scenarios and include scenario-dependent warming trends and sea-ice declines.

For SIC, the following procedure is adopted. Under the NW climate, SIC in the Northern Hemisphere (NH) is estimated using SST together with the observed relationship between SST and SIC, whereas SIC in the Southern Hemisphere (SH) is prescribed directly from the observation-based dataset. For the future climate, SIC is prescribed such that the resulting sea ice area (SIA) is consistent with CMIP6 future projections. As in the NW climate, the SST–SIC relationship is applied to estimate SIC in the NH, while SIC in the SH is represented by a retreat of the observation-based SIC.

Overall, the bias-corrected datasets provide a comprehensive basis for evaluating impacts of anthropogenic warming using coupled models with ocean data assimilation and enable a robust quantitative assessment of coupled climate responses and uncertainties in future projections,

thereby contributing to climate adaptation strategies. Note that these upper-ocean datasets were developed for assimilation into MRI-ESM2-0 as part of an effort to construct datasets complementary to d4PDF, which ensures a realistic representation of upper-ocean conditions while preserving atmosphere–ocean coupling in future climate simulations. Accordingly, the selection of emission scenarios, the adjustment of climate sensitivity across CMIP6 models, and the representation of uncertainties, as described in the Methods section, are affected by the experimental design of the future projection simulations in our effort to produce complementary climate projection datasets. Nevertheless, this experimental framework is widely applicable to efforts to construct climate projection datasets by other groups. The upper-ocean data presented here can be applied to ocean-data-constrained CGCMs or ESMs with similar protocols, as well as to atmospheric general circulation models (AGCMs) that use SST and SIC as boundary conditions.

Method

This section describes the methodological framework used to construct the upper-ocean dataset. It begins with a description of the experimental design for generating a new climatological dataset based on the MRI-ESM2-0 with ocean data assimilation. This is followed by a description of the baseline datasets used to construct the upper-ocean dataset. The section then describes the procedures used to construct the upper-ocean temperature and salinity dataset for the NW and future climates. The procedure to estimate SIC for the NW and future climates is described separately. In addition, a region-specific bias correction applied to the Japan Sea is explained.

Experimental design for a new climate projection dataset using an ESM assimilating the upper ocean datasets described in this study

To specify the requirements for constructing upper-ocean data, we briefly introduce the experimental design for developing the next-generation climate assessment dataset using the climate simulations based on the MRI-ESM2-0 with ocean data assimilation.

The externally forced changes follow the CMIP6 protocol and include those from the historical[44], hist-nat[45], and SSP[46] simulations. The present-climate experiment covers the period 1961–2020, using historical forcings from 1961 to 2014 and SSP2-4.5 forcings from 2015 to 2020 (see Mizuta et al.[43] for details). For the present climate, temperature, salinity, and SIC

are assimilated into MRI-ESM2-0, where temperature and salinity are taken from a monthly observation-based objective analysis of Ishii et al.[47] and SIC from the monthly COBE-SST2 dataset[48]. Although temperature and salinity data are available down to 3000 m, assimilation is applied only to the upper 500 m.

In addition to the present climate experiment, NW and future climate simulations are performed. The NW experiment is driven by the CMIP6 hist-nat forcing, requiring upper-ocean data with warming levels consistent with the pre-industrial climate. In the future climate, uncertainty arises from scenarios, inter-model differences, and internal variability. To address the scenario uncertainty, three SSP scenarios (SSP1-2.6, SSP2-4.5, and SSP5-8.5) are used. To address the model uncertainty, anthropogenic externally forced changes in the upper ocean are extracted from multiple CMIP6 models. Because several CMIP6 models exhibit high climate sensitivity[49,50], the climate sensitivity under SSP5-8.5 is adjusted so that the simulated GMSAT is consistent with the assessed warming reported in IPCC AR6[51]. For SSP1-2.6 and SSP2-4.5, the climate sensitivity is not adjusted, but models with warming exceeding the assessed range of IPCC AR6[51] are excluded. As described later, the future climate simulations are performed by shifting the phase of internal variability estimated by extracting the forced trend from the observation-based objective analysis, thereby accounting for the uncertainty associated with internal variability.

Baseline data

Following previous studies[18,19,20], NW and future projection datasets are generated by correcting biases of CMIP simulations, in which the CMIP-projected externally forced change is subtracted from or added to the observation-based present-climate dataset. This subsection describes the observation-based datasets and CMIP model outputs used for the construction of the NW and future projection datasets.

As an observed baseline for the present climate, the monthly observation-based objective analysis of temperature and salinity from Ishii et al.[47] (`https://climate.mri-jma.go.jp/pub/ocean/ts/v7.3.1`) is used except in the Japan Sea, where a four-dimensional variational ocean reanalysis for the Western North Pacific over 30 years (FORA-WNP30)[52] (`https://search.diasjp.net/en/dataset/FORA_WNP30_JAMSTEC_MRI`) is additionally used to correct biases of Ishii et al.[47] as described later. The SIC is based on COBE-SST2[48] (`https://climate.mri-jma.go.jp/pub/ocean/cobe-sst2`) whose SST is consistent with that of Ishii et al.[47] These

observation-based datasets are the same as those used in the MRI-ESM2-0 simulations with ocean data assimilation in the present climate[43]. For comparison, Extended Reconstructed SST version 5 (ERSSTv5)[53], the Met Office Hadley Centre's sea ice and SST data set version 1 (HadISST1)[54], and the Met Office Hadley Centre SST data set version 4 (HadSST4)[55] are also utilized.

To estimate externally forced changes, temperature, salinity, and SIC from CMIP6 models are used. To account for uncertainty in future scenario projections, three scenarios, SSP1-2.6, SSP2-4.5, and SSP5-8.5, are considered. To address uncertainty arising from differences among models, multiple CMIP6 models are used. However, as ensemble means are taken for each model to minimize effect of internal variability before extracting externally forced trends, only models with at least four ensemble members for all historical and future scenarios are selected. Additionally, the results of the piControl experiment are used to estimate the S/N ratio of externally forced changes. All CMIP6 model outputs are horizontally regridded onto a $1^\circ \times 1^\circ$ grid using Climate Data Opetators (CDO)[56] to be consistent with the temperature and salinity data of Ishii et al.[47] and COBE-SST2. In the vertical direction, the data are linearly interpolated to the levels of Ishii et al.[47] (The final product is provided on the vertical grid of the ocean component of MRI-ESM2-0, obtained through vertical interpolation.) To focus on the coupling process between the atmosphere and ocean, only upper-ocean temperature and salinity above 500 m are used for assimilation in the climate simulations while the NW and future climate datasets are reconstructed to the depth of 3000 m.

Based on these conditions, nine models listed in Table 1 are used. The data of these models can be accessed from the website of ESGF (`https://esgf-node.llnl.gov/search/cmip6`). The table also indicates the number of ensemble members used for the ensemble averages. The selected CMIP6 models employ different AGCMs and ocean general circulation models. This diversity of models can lead to a larger inter-model spread and enables a more comprehensive assessment of model uncertainty.

Procedure to create the data for temperature and salinity for NW and future

This subsection details the procedures to construct the upper-ocean temperature and salinity, while the procedure for SIC is presented in the next subsection.

Decomposition of temperature and salinity

The ocean temperature (θ) and salinity (S) are decomposed into three components: (i) the present-day monthly climatology (θ_c, S_c), (ii) internal variability (θ_i, S_i), and (iii) externally forced changes (θ_f, S_f). This decomposition follows

$$\theta = \theta_c + \theta_i + \theta_f, \tag{1}$$

$$S = S_c + S_i + S_f. \tag{2}$$

The climatologies are defined as the 1961–2020 averages of observation-based temperature (θ^o) and salinity (S^o):

$$\theta_c \equiv \langle \theta^o \rangle_{1961-2020}, \quad S_c \equiv \langle S^o \rangle_{1961-2020}, \tag{3}$$

where brackets ($\langle\ \rangle$) denote the climatological mean for each month. The internal variability components are obtained as the residual after removing the climatology and the externally forced change in the present climate (θ_f^H, S_f^H) from the observation-based dataset:

$$\theta_i = \theta^o - \theta_c - \theta_f^H, \tag{4}$$

$$S_i = S^o - S_c - S_f^H. \tag{5}$$

Taking the climatological mean of Eqs. (4) and (5) over 1961–2020 constrains the climatological means of the internal variability and externally forced change. Here, these climatological means are defined as

$$\langle \theta_i \rangle_{1961-2020} = -\langle \theta_f^H \rangle_{1961-2020} = 0, \tag{6}$$

$$\langle S_i \rangle_{1961-2020} = -\langle S_f^H \rangle_{1961-2020} = 0. \tag{7}$$

Throughout this study, we assume that the externally forced change does not modify the statistical properties of internal variability. Consequently, the internal variability derived from the present climate is used in both the NW and future climates.

Internal variability in the future climate

Internal variability in 1961–2020 is imposed cyclically in the future simulations. The January–December internal variability of 2021 is linearly transitioned within one year to that of

1961 through a weighted average between 2021 and 1961. In our future experiment design, however, the phase of the internal variability is shifted when transitioning from the present to future climates, in order to represent unpredictable future internal variability using ensemble simulations. Specifically, in model year 2021, the internal variability does not only transition to that of 1961 but also to that of 1971, 1981, 1991, 2001, or 2011. In subsequent years, once the internal variability reaches that of 2021, it again transitions from 2021 to 1961. For example, if the internal variability transitions from 2021 to 1961 in model year 2021, then the internal variability again transitions from 2021 to 1961 in model year 2081:

Model year:	1961	- - -	2021	- - -	2081	- - -	2100
Year of the internal variability:	1961	- - -	2021				
			1961	- - -	2021		
					1961	- - -	1980

On the other hand, if the internal variability transitions from 2021 to 2011 in model year 2021, then the transitions occur from 2021 to 1961 in model years 2031 and 2091:

Model year:	1961	- - -	2021	- - -	2031	- - -	2091	- - -	2100
Year of the internal variability:	1961	- - -	2021						
			2011	- - -	2021				
					1961	- - -	2021		
							1961	- - -	1970

These six ensemble members can represent 60 years' worth of internal variability for any arbitrary 10-year period in future simulations.

Extraction of externally forced SST modes

Because we recognize that it is challenging to completely disentangle forced and natural variability in observation-based time series, we used a temporally smoothed ensemble mean to suppress natural variability as much as possible before estimating externally forced variability from CMIP6 models. Specifically, a first-order Butterworth low-pass filter with a cutoff period of 10 years is applied to the ensemble mean temperature and salinity of each model. Because SST has the largest impact on the atmosphere among the variables considered, we extract the EOF modes that maximize the horizontally averaged variance of the SST.

Using the anomaly matrix of the low-pass filtered ensemble mean SST from the temporal average (A), the diagonal weight matrix (W), and the number of years (N_t), the weighted $N_i \times N_i$

covariance matrix is calculated as $V \equiv WA^TAW/(N_t-1)$, and the EOF mode is obtained by solving the eigenvalue problem

$$Vx'_n = \lambda_n x'_n, \tag{8}$$

where λ_n and x'_n are the eigenvalue and eigenvector of mode n, respectively[57]. Since the CMIP SST data are regridded to a $1^\circ \times 1^\circ$ grid, the total number of grid cells (N_i) is 180×360 ($i = 1, 2, \ldots, 180 \times 360$). The diagonal elements of W is defined as $\sqrt{w_i/\Sigma w_i}$, where the grid weight is given by $w_i = R^2(\pi/180)^2 \cos\phi_i$, R ($= 6.375 \times 10^6$ m) is the Earth's radius, and ϕ_i is the latitude of each grid cell. Land points are assigned a weight of zero ($w_i = 0$). The number of years (N_t) is 171 for 1855–2025 in the present climate and 101 for 1995–2095 in the future climate. The eigenvector x'_n is normalized ($x'^T_n x'_n = 1$).

The SST anomaly of each mode (A_n) is given by

$$A_n = \sqrt{\lambda_n} t_n x_n^T = \frac{t_n t_n^T A}{N_t - 1} = AWx'_n x'^T_n W^{-1}, \tag{9}$$

where $x_n = W^{-1}x'_n = A^T t_n/[\sqrt{\lambda_n}(N_t-1)]$ and $t_n = AWx'_n/\sqrt{\lambda_n}$. The spatial pattern of the EOF (x_n) is related to the covariance matrix between the A and A_n as

$$\frac{A^T A_n}{N_t - 1} = \sqrt{\lambda_n}\frac{A^T t_n x_n^T}{N_t - 1} = \lambda_n x_n x_n^T. \tag{10}$$

Thus, $\lambda_n x_n x_n^T$ represents the covariance matrix between SST anomaly and its EOF mode. The time series of the principal component (PC) is normalized such that $t_n^T t_n/(N_t-1) = 1$. Furthermore, the horizontally averaged variance of A_n is obtained as

$$\mathrm{tr}\left(\frac{WA_n^T A_n W}{N_t - 1}\right) = \mathrm{tr}\left(x'_n x'^T_n V x'^T_n x_n\right) = \lambda_n, \tag{11}$$

using Eqs. (8) and (9). Thus, the eigenvalue λ_n is the horizontally averaged variance of mode n of the EOF of the SST.

These EOF modes contain contributions from both internal and external variability. To identify the modes primarily associated with externally forced changes, we estimate the variance of internal variability for each mode (λ_n^{pic}) using piControl simulations. Specifically, the spatial pattern of each EOF mode is projected onto the linearly detrended low-pass-filtered SST anomaly

from the piControl simulation ($A^{\rm pic}$). Using $A^{\rm pic}$, the number of years in the piControl simulation ($N_t^{\rm pic}$), and the number of ensemble members for each model in the present and future climates (N_e), the variance attributable to internal variability is calculated as

$$\lambda_n^{\rm pic} = \frac{(A^{\rm pic} W x_n')^T A^{\rm pic} W x_n'}{N_e (N_t^{\rm pic} - 2)}. \tag{12}$$

A mode is classified as being dominated by externally forced changes when the S/N ratio, defined as $(\lambda_n - \lambda_n^{\rm pic})/\lambda_n^{\rm pic}$, exceeds 10.

Externally forced changes of the temperature and salinity

For each externally forced mode, its PC (t_n) is projected onto anomaly matrices of temperature (θ_A) and salinity (S_A). The anomalies are taken from the averaged value between 1855 and 2025 in the present climate and between 1995 and 2095 in the future climate. Then, the spatial pattern of the temperature $[\theta_A^T t_n/(N_t - 1)]$ and salinity $[S_A^T t_n/(N_t - 1)]$ are derived, and the externally forced mode of n of model m of temperature (θ_{mn}) and salinity (S_{mn}) is calculated as

$$\theta_{mn} = t_n' t_n^T \theta_A/(N_t - 1), \tag{13}$$

$$S_{mn} = t_n' t_n^T S_A/(N_t - 1). \tag{14}$$

Here, t_n' is the extended time series of the PC. Since t_n is defined between 1855 and 2025 for the present climate or between 1995 and 2095 for the future climate, time series from 1850 to 1854 or from 2096 to 2100 is estimated using the eigenvector of each SST EOF mode (x_n') and its projection onto ensemble mean SST anomalies without temporal filter (A') as $A' W x_n'/\sqrt{\lambda_n}$. By appending this time series to t_n, t_n' is obtained.

Present-climate externally forced change and sensitivity adjustment

In the present climate, externally forced changes of temperature (θ_f^H) and salinity (S_f^H) are obtained as a combination of the multi-model averaged externally forced modes as

$$\theta_f^H = \frac{1}{N_m} \sum_m \beta_m^H \sum_n \left(\theta_{mn}^H - < \theta_{mn}^H >_{1961-2020} \right), \tag{15}$$

$$S_f^H = \frac{1}{N_m} \sum_m \beta_m^H \sum_n \left(S_{mn}^H - < S_{mn}^H >_{1961-2020} \right), \tag{16}$$

where N_m is the number of models and β_m^H is the present climate adjustment coefficient. The externally forced changes are anomalies from the averaged value in 1961–2020 because the climatology of externally forced change in the present climate is set to be zero as in Eqs. (6) and (7).

The coefficient of β_m is used to adjust the climate sensitivity of each model. In the present climate, the linear trend of the GMSST in 1961–2020 in each model is adjusted to be the same as that of the observation-based dataset to minimize the bias derived from the climate sensitivity bias in models. Figure 1a-i shows the time series of the GMSST of observation-based dataset (thin black lines), CMIP6 models (red lines), and sensitivity-adjusted externally forced changes (green lines). The SST changes over 1961–2020 are larger than that observed in some models (e.g., CanESM5 in Fig. 1d and UKESM1-0-LL in Fig. 1i). The linear trend of the GMSST calculated from least-squares fitting is also shown in Fig. 1k. Except for MIROC6, the linear trend is overestimated in the CMIP6 models compared with COBE-SST2 (khaki bar in Fig. 1k) while the ensemble spread of CNRM-CM6-1 and MPI-ESM1-2-LR captures the trend estimated from COBE-SST2.

NW and future externally forced components

Since the mean externally forced changes for the period 1961–2020 are defined as zero, those for the NW period (1850–1899)

$$\theta_f = < \theta_f^H >_{1850-1899}, \tag{17}$$

$$S_f = < S_f^H >_{1850-1899} \tag{18}$$

represent the changes relative to the 1961-2020 mean. Note that their negatives can be interpreted as the mean externally forced changes supposed to be contained in the objective analysis data for 1961-2020.

The future externally forced changes of the temperature (θ_f^S) and salinity (S_f^S), on the other hand, are

$$\theta_f^S = < \theta_f^H >_{1995-2014} + \beta_m^S \sum_n \left(\theta_{mn}^S - < \theta_{mn}^S >_{1995-2014} \right), \tag{19}$$

$$S_f^S = < S_f^H >_{1995-2014} + \beta_m^S \sum_n \left(S_{mn}^S - < S_{mn}^S >_{1995-2014} \right), \tag{20}$$

and multi-model averaged externally forced changes are

$$\theta_f^S = < \theta_f^H >_{1995-2014} + \frac{1}{N_m} \sum_m \beta_m^S \sum_n \left(\theta_{mn}^S - < \theta_{mn}^S >_{1995-2014} \right), \quad (21)$$

$$S_f^S = < S_f^H >_{1995-2014} + \frac{1}{N_m} \sum_m \beta_m^S \sum_n \left(S_{mn}^S - < S_{mn}^S >_{1995-2014} \right). \quad (22)$$

When adjusting climate sensitivity, we use the assessed warming values provided in IPCC AR6 as a reference (Table 4.5 of the IPCC AR6 WG1 Full Report[51]).

Figure 2 shows the difference in annual mean GMSST and GMSAT between 1995–2014 and 2081–2100. For GMSAT, the central estimates of the assessed warming ($\Delta\mathrm{SAT_A}$, gray circles) and their uncertainty ranges (error bars) are also indicated. The GMSAT increase (ΔSAT) relative to the GMSST increase (ΔSST) shows relatively small inter-model dependence compared to the inter-model spread of the climate sensitivity, and their multi-model mean is 1.4 with a small standard deviation of 0.060 [$\Delta\mathrm{SAT} = (1.4 \pm 0.060)\Delta\mathrm{SST}$]. This indicates that inter-model differences in ΔSAT primarily determined from differences in ΔSST, while the SST–SAT relationship itself is broadly consistent across models. Therefore, to obtain SST changes consistent with the assessed warming in terms of GMSAT, the SST change in each model is scaled by the ratio of the assessed to the model-specific GMSAT increase (i.e., $\beta_m^S = \Delta\mathrm{SAT_A}/\Delta\mathrm{SAT}$). For SSP1-2.6 and SSP2-4.5, some models (ACCESS-CM2, CanESM5, and UKESM1-0-LL) exhibit higher climate sensitivity, exceeding the assessed warming range. Since our experimental design does not adjust climate sensitivity for these scenarios (i.e., $\beta_m^S = 1$), these three models are excluded. For SSP5-8.5, however, sensitivity adjustment is applied using the central estimate of the assessed warming ($\Delta\mathrm{SAT_A} = 3.5$ °C), and thus all nine models are included in the experiments, along with a multi-model mean constructed from the adjusted results. All future experiments are referenced to the assessed warming relative to 1995–2014.

Temporal transition from present to future climates

The warming levels of the externally forced changes are adjusted so that they are identical in 1995–2014 between the present and future climates as

$$< \theta_f^S >_{1995-2014} = < \theta_f^H >_{1995-2014}, \quad (23)$$

$$< S_f^S >_{1995-2014} = < S_f^H >_{1995-2014}. \quad (24)$$

Time sequential externally forced changes from the present to future climates are

$$\theta_f = (1-\alpha)\theta_f^H + \alpha\theta_f^S, \tag{25}$$

$$S_f = (1-\alpha)S_f^H + \alpha S_f^S. \tag{26}$$

The weighting function α is defined as

$$\alpha = \begin{cases} 0 & Y \leq 2020 \\ \dfrac{12(Y-2021)+M-0.5}{60} & 2021 \leq Y \leq 2025 \\ 1 & 2026 \leq Y. \end{cases} \tag{27}$$

Here, Y and M denote the year and month (1–12) in the simulations. The duration of the transition of the externally forced change from the present to future climates is five years.

Procedure to create the data for SIC for NW and future

NW climate

In the NW climate, NH SIC is prescribed following the d4PDF approach[20]. The NH SIC (I) is diagnosed from the SST as

$$a^H I^2 + b^H I + c^H = \theta(z=0), \tag{28}$$

where $\theta(z=0)$ is the SST. The coefficients a^H, b^H, and c^H are identical to those used in COBE-SST2[48]. They vary spatially and exhibit seasonal dependence, but do not change from year to year. However, in the SH, this method may lead to less realistic SIC distributions as described later, and thus a different approach from that used in the NH is applied.

In the NH, the SIA exhibits a clear decreasing trend during the satellite era (Fig. 3a). Based on COBE-SST2, linear trends of monthly mean SIA calculated by least-squares fitting for the period 1978–2020 show negative values in all months, ranging from a minimum of -0.76×10^{12} m^2 decade^{-1} in September to a maximum of -0.28×10^{12} m^2 decade^{-1} in January. These pronounced declines imply that NH sea ice has experienced substantial externally forced changes since the onset of satellite observations. The method based on Eq. (28) can represent the increase in SIC associated with SST cooling in the NW climate as described in the following

section. In contrast, the SH SIA derived from COBE-SST2 shows little evidence of a long-term decreasing trend during the satellite era (Fig. 3b). The linear trends for 1978–2020, unlike those in the NH, are not negative and range from 0.057×10^{12} m^2 decade^{-1} in November to 0.23×10^{12} m^2 decade^{-1} in June. This weak trend suggests that the externally forced change in SH SIC is considerably smaller than in the NH in the present climate.

In this study, we therefore assume that the externally forced change in SH SIA associated with global warming is negligible compared with that in the NH. Accordingly, for the NW climate, SH SIC is prescribed using observation-based SIC from COBE-SST2. This approach allows realistic month-to-month and year-to-year variability to be represented in SH SIC while avoiding the imposition of an artificial long-term trend associated with global warming.

Future climate

In the future climate, SIC is prescribed so that the SIA is consistent with CMIP6 future projections. The hemispheric SIA (E) is obtained from the observation-based and modeled climatologies in recent past and the future projected changes as

$$E = \frac{E_f^m}{E_c^m} E_c^o, \tag{29}$$

where E_c^o is the observation-based monthly climatology of SIA for 1995–2014, E_c^m is the corresponding climatology from each CMIP6 model, and E_f^m is the future SIA from each model smoothed using a first-order Butterworth low-pass filter with a 10-year cutoff period. Under SSP5-8.5, the ratio E_f^m/E_c^m is taken from the multi-model mean because climate sensitivity is adjusted in this scenario.

In the NH, SIC is diagnosed from SST using a relationship,

$$a^S I^2 + c^S = \theta(z = 0), \tag{30}$$

where

$$a^S = a_0^S \left(1 - I^2\right) + a_1^S I^2, \tag{31}$$

$$c^S = c_0^S \left(1 - I^2\right) + c_1^S I^2, \tag{32}$$

with coefficients a_0^S, a_1^S, c_0^S, and c_1^S that are independent of location but vary in time. These

coefficients are determined to satisfy the following conditions:

$$a^S I_0^2 + c^S = \theta_c(z=0) + \theta_f(z=0), \tag{33}$$

$$E = \iint I_0 \, dx \, dy, \tag{34}$$

where I_0 is the SIC without internal variability.

For $I_0 = 1$, the left-hand side of Eq. (33) corresponds to the freezing-point temperature. Because the freezing temperature is proportional to salinity, it is expressed as mS_{fr}, where S_{fr} is the sea surface salinity (SSS) without internal variability $[S_c(z=0) + S_f(z=0)]$ averaged over NH grid points with $0.85 < I_0 < 1.0$ (if unavailable, grid points with $0.15 < I_0 < 0.85$ are used; if those are also unavailable, grid points with $0 < I_0 < 0.15$ are used), and $m = -0.0543$ °C psu^{-1} [58,59] to be consistent with the setting for the ocean component of MRI-ESM2-0 [60]. Accordingly, c_1^S is given by

$$c_1^S = -a_1^S + mS_{fr}. \tag{35}$$

First, using the 20-year mean SIC and SST from COBE-SST2 for 1995–2014, the coefficients a_0^S, a_1^S, c_0^S, and c_1^S are estimated by least-squares fitting under the constraints $a^S = a_0^S = a_1^S$ and $c^S = c_0^S = c_1^S$. These coefficients are used as initial values for the subsequent iterative adjustment. In the first step of the iteration, the parameter c_0^S is varied within the range -2 °C $\leq c_0^S \leq 2\cos[\pi(M-9)/12]$ °C, and the value that minimizes the difference between the target SIA (E) and the SIA estimated from the diagnosed SIC ($E_{\rm est}$) is selected. If $|E_{\rm est}-E|/E > 10^{-3}$ and $E_{\rm est} > E$, a_1^S is reduced by 5%. If $|E_{\rm est}-E|/E > 10^{-3}$ and $E_{\rm est} < E$, a_1^S is increased by 5%. After each adjustment of a_1^S, c_0^S is re-optimized in the same manner. Next, a_0^S is adjusted in the opposite sense: if $E_{\rm est} > E$, a_0^S is increased by 5%, and if $E_{\rm est} < E$, a_0^S is reduced by 5%. This step is again followed by a readjustment of c_0^S. These adjustments of a_1^S and a_0^S, together with the re-optimization of c_0^S, are repeated until $|E_{\rm est}-E|/E < 10^{-3}$ is satisfied.

In the SH, we do not estimate SIC from SST for future because preliminary application of the method resulted in an implausible SIC distributions owing to the poor performance of CMIP6 models in terms of SIC distribution in the Southern Ocean. For example, some models underestimate Antarctic sea ice relative to observation-based datasets. Since future SST changes are particularly pronounced around the marginal sea-ice zones of the present climate, enhanced warming is expected near Antarctica in models with smaller present-day sea-ice extent. The gap between the observation-based dataset and CMIP6 output can lead to physically implausible

patterns of SST change, such as sea ice forming only on the equatorward side when SST decreases equatorward (resulting in colder waters on the equatorward side than near the pole). For these reasons, future SIC is derived by reducing the monthly mean SIC for 1995–2014 from the outer margins inward until the SIA reaches E in Eq. (29) using horizontal smoothing based on the central grid point and its four adjacent neighbors, with the central value weighted according to the number of valid neighboring grid points. When the smoothed SIC falls below 0.15, it is set to zero. Smoothing is not applied to grid points where SIC exceeds 0.85 after smoothing. Antarctic coastal grid points whose values are lower than those of surrounding points are excluded from the smoothing procedure. For MIROC6, the SH SIA does not decrease relative to the present climate (Fig. 3d,f,h) because the SIA in the present climate is already small for this model. Therefore, for this model, the multi-model mean ratio E_f^m/E_c^m is used instead of the individual model estimate.

Bias correction in the Japan Sea

In the Japan Sea, particularly along the northern Japanese coast, the SST climatology of Ishii et al.[47], which is nearly identical to COBE-SST2 (Fig. 4a), exhibits discrepancies exceeding 1 °C relative to the satellite-based dataset of the merged satellite and in situ data Global Daily SST (MGDSST)[61] (Fig. 4b). Because an SST difference of about 1 °C in the Japan Sea can substantially affect the Japanese climate and weather[62,63,64], we applied a bias correction to the temperature and salinity there. However, MGDSST does not provide subsurface temperature or salinity. To address this, we used FORA-WNP30, a high-resolution ($\sim$ 10 km) ocean reanalysis for the northwestern Pacific that assimilates MGDSST and achieves similar reproducibility. In fact, the differences between the objective analysis of Ishii et al.[47] and MGDSST almost coincide with the differences between that of Ishii et al.[47] and FORA-WNP30 (Fig. 4b,c). It should be noted that the FORA-WNP30 dataset spans only 1982–2016, and thus does not fully cover the present climate (1961–2020) considered in this study. To overcome this limitation, we corrected biases by adding the monthly climatological differences in temperature and salinity between the objective analysis of Ishii et al.[47] and FORA-WNP30 over 1982–2016, as shown in Fig. 4c, to that of Ishii et al.[47] in the Japan Sea.

Data Records

The dataset is available from the MRI data server at `https://climate.mri-jma.go.jp/pub/archives/Ushijima-et-al_Upper_Ocean_Data`. Metadata, documentation, and citation information for the dataset are archived through Zenodo[65].

For the NW climate, the data are stored in the NW directory. For the future climate, the SSP126, SSP245, and SSP585 directories contain data for each scenario. Within each SSP directory, subdirectories are organized by the CMIP6 model and the phase of internal variability. The directory names v00, v10, v20, v30, v40, and v50 correspond to transition years of internal variability in 1961, 1971, 1981, 1991, 2001, and 2011, respectively, which are aligned to model year 2021.

In each directory, temperature and salinity data (ProjD-7.5_1x1_YYYY.grb2), SIC data (cobe-sic2_1x1_YYYY.grb2), as well as the perturbation data for SST (cobe-sst2_ptb_1x1_YYYY.grb2) and SIC (cobe-sic2_ptb_1x1_YYYY.grb2) are provided. The perturbation data are included to generate a larger spread of internally generated atmospheric variability. Details of the perturbation method are described in Mizuta et al.[20] Here, YYYY denotes the year of the data. All data are provided in GRIB version 2 format, and a corresponding GrADS control file (.ctl) is available for each GRIB file. Additional information on the directory structure, file formats, and variables is provided in the accompanying documentation archived through Zenodo.

Technical Validation

The developed upper-ocean dataset, including temperature, salinity, and SIC, is presented here. Temperature and salinity are examined first, followed by SIC.

NW and Future Temperature and Salinity

The temperature and salinity components of the upper-ocean dataset are evaluated for externally forced changes in the present climate. Internal variability is then assessed, and the datasets under NW and future climate conditions are further examined.

Externally Forced Changes in Present Climate

The externally forced change derived from the multi-model mean is evaluated in the present climate. The evaluation focuses on the EOF-based extraction of SST changes.

Externally forced changes in the present climate are derived from the EOF analysis of CMIP6 SST. Figure 5 shows the spatial patterns (x_1, x_2) and extended PCs (t'_1, t'_2) of the first and second EOF modes of February SST for each model. The spatial patterns of the first EOF modes of all models show positive distributions across most regions (Fig. 5a–i). Their PCs (t'_1) exhibit similar temporal evolutions across all models, characterized by nearly monotonic increases that become more pronounced after the 1970s (Fig. 5j). These features indicate that the first EOF mode primarily represents a warming trend.

In the Arctic Ocean, all models exhibit small changes compared to other regions due to the sea ice in February, which keeps the temperature near the freezing point. As sea ice extent varies seasonally, the first EOF mode in August shows an expanded positive distribution around the Arctic Ocean compared to February (Fig. 6a–i), indicating seasonal variations in the warming trend of the SST. In addition, a comparison of the first EOF modes in February and August indicates that the warming tends to be stronger in the summer hemisphere. This is likely due to the shallower mixed layer depth in summer, which leads to a larger thermal response to warming[66]. Although the overall spatial patterns are consistent and the temporal evolution is nearly identical between February and August (Figs. 5a–j and 6a–j), the seasonal cycle of the externally forced change needs to be taken into account.

Table 2 presents the annual mean explained variance and S/N ratio for each mode in the EOF analysis of the models. The first mode is dominant across all models, explaining more than 77% of the total variance, and it exhibits a high S/N ratio (S/N ratio $> 0.82 \times 10^2$), indicating it as a mode dominated by externally forced changes.

The PCs of the second modes of SSTs in February and August show increasing trends until the 1980s and decreasing trends thereafter in most models, except for CNRM-CM6-1 and IPSL-CM6A-LR in February (Figs. 5t and 6t), in which decreasing trends are observed during 1850–1870 and 1890–1960, respectively. The spatial pattern is negative in the mid-latitudes of the NH and positive in other regions (Figs. 5k,l,n,p–s and 6k–s), showing overall consistency among the models. The NH mid-latitude cooling observed in the second mode until the 1980s, followed by enhanced warming thereafter, can be attributed to the temporal evolution of anthropogenic aerosol emissions[67]. This mode explains about 10% of the variance in some models (CESM2, MRI-ESM2-0, and UKESM1-0-LL), and its S/N ratio exceeds 10 in most models, except for CNRM-CM6-1 and IPSL-CM6A-LR (Table 2). Thus, both the first and second modes are considered externally forced modes, provided the S/N ratio of the second mode exceeds 10 as

described in the Method section. The S/N ratio of the third mode is below 10 in most models. Although MIROC6 shows an S/N ratio exceeding 10, the explained variance is only 0.72%. Therefore, third and higher modes of the EOF are excluded from the analysis of externally forced change.

Internal variability

The internal variability of the temperature (θ_i) and salinity (S_i) is obtained as the residuals after removing the climatology and externally forced change from the observation-based dataset. Figure 7 shows the first and second EOF modes of the internal variability of the SST. The first EOF modes has the ENSO-like spatial pattern (Fig. 7a). The corresponding PC time series captures major El Niño events, including those of 1982/83, 1991/92, and 1997/98[68] (Fig. 7c). The second mode exhibits variability primarily concentrated in the tropical and North Pacific Ocean (Fig. 7b). These results indicate that the datasets retain tropical Pacific internal variability, including ENSO-like variability, under both the NW and future climates.

NW climate

For the purpose of evaluating the impact of anthropogenic global warming under the present climate, NW simulations are useful. The temperature and salinity in the NW climate are constructed based on the objective analysis in the present climate, together with the climatological differences between 1850–1899 and 1961–2020 [Eqs. (17) and (18)]. Note that temporal changes in temperature and salinity due to external forcing are not considered in the NW simulation. Accordingly, temperature and salinity for the NW period are obtained as the sum of the NW climatological mean state and the internal variability.

Figure 8 shows the externally forced changes in the climatological temperature and salinity difference between 1850–1899 and 1961–2020. Except for parts of the Southern Ocean, the SST in the NW climate decreases compared to the present climate (Fig. 8a), with a global mean decrease of 0.37 °C. In COBE-SST2, the difference in the GMSST between 1850–1899 and 1961–2020 is −0.38 °C, with a difference of −0.015 °C from the multi-model mean. Among the observation-based datasets, COBE-SST2 exhibits higher SST prior to 1900 compared to the present climate (Fig. 1j). As a result, the multi-model mean GMSST is slightly higher than that derived from the observation-based datasets. However, differences in GMSST among the observation-based datasets before 1900 are on the order of 0.1 °C, and the difference between

COBE-SST2 and the multi-model mean is smaller than the inter-dataset spread.

Compared to the present climate, the observation-based SST in 1850–1899 is warmer not only in parts of the Southern Ocean but also in parts of the North Atlantic (Fig. 8b). The NW SST estimated from the multi-model mean exhibits negative deviations relative to COBE-SST2 in parts of the North Atlantic and around Antarctica, and positive deviations over many regions in the mid-latitudes, particularly around the western boundaries (Fig. 8c).

The NW externally forced changes in interior temperature and salinity were estimated by projecting the PCs of each externally forced SST mode onto temperature and salinity anomalies. Compared with the present climate, temperatures at 300 m in the NW climate are higher equatorward of 30°S and lower over most of the remaining regions (Fig. 8d). The SSS is positive in most regions but negative in the North Atlantic (Fig. 8e). The increase in the SSS in the Arctic region is likely related to the increase in the SIC.

Future climate

As in the present climate analysis, externally forced change was extracted in the future climate experiments using EOF analysis. For SSP1-2.6 and SSP2-4.5, the ACCESS-CM2, CanESM5, and UKESM1-0-LL were excluded because of their high climate sensitivity exceeding the range (Fig. 2) estimated from multiple lines of evidence reported in IPCC AR6[51]. In contrast, for SSP5-8.5, all models were used because the experiment is designed with adjusted climate sensitivity.

Figures 9–11 show the first and second EOF modes of the SST for SSP1-2.6, SSP2-4.5, and SSP5-8.5. Similar to the present climate, the first mode is dominant, with contributions exceeding 88% for SSP1-2.6 (Table 3), 95% for SSP2-4.5 (Table 4), and 98% for SSP5-8.5 (Table 5). The spatial patterns of the first mode are similar across scenarios, characterized by positive anomalies over most regions except for the North Atlantic Ocean (40°–60°N and 0°–60°W), and the PCs increase with time. These indicate that this mode represents global warming. The associated trends, however, differ across scenarios: nearly linear warming for SSP2-4.5, and a cessation and an acceleration in warming after the mid-21st century for SSP1-2.6 and SSP5-8.5, respectively. Among the CMIP6 models used, the first modes of the PCs are highly consistent, and their spatial patterns also roughly agree, although differences exist in the North Atlantic and in the tropical Pacific.

The second EOF mode also exhibits similar temporal evolution across models and scenarios,

with an increase until the mid-21st century followed by a decline thereafter. Although the contribution of the second mode is small under SSP2-4.5 and SSP5-8.5 scenarios, it is about 10% in MRI-ESM2-0 under SSP1-2.6, as in the present climate (Tables 2–5). For SSP1-2.6, three models (CNRM-CM6-1, MIROC6, and MRI-ESM2-0) with contributions exceeding 5%, as well as CESM2, exhibit positive anomalies except in the Southern Ocean. In these models, the second mode slightly increases the GMSST until the mid-21st century and decreases it thereafter. Figure 12 shows the GMSST time series for each scenario, illustrating that under SSP1-2.6, some models project a decrease in the GMSST after the mid-21st century. The S/N ratio exceeds 10 for both the first and second modes in all models (Tables 3–5). Thus, both modes are treated as externally forced modes. The third mode, with contributions below 1.4%, is not included as a forced mode.

Here, the evolution of the GMSST in MRI-ESM2-0 from the present to future climates is also shown in Fig. 12. As described in Eq. (27), the externally forced change transitions gradually from the present climate (1855–2025, black dashed lines) to the future climate (1995–2095, lime-colored dashed lines) during the period 2021–2025. The detailed procedure for this transition is described in the Method section.

NW and Future SIC Data

NW climate

SIC in the NW climate is examined to evaluate its spatial distribution. In the NH, the SIC is derived from the SST using the empirical coefficients employed in COBE-SST2, as described in the Method section. Figure 13 shows the SIC in the present and NW climates. Compared with the present climate, the February sea ice extent is slightly larger in the NW climate. Although the spatial patterns are generally similar from year to year, minor differences are found, such as sea ice extension from the Bering Strait into the Pacific Ocean. In contrast, August SIC in the present climate shows a gradual declining trend from 1970 to 2010, whereas such a declining tendency is not evident in the NW climate, despite some variations associated with internal variability.

In the SH, NW SIC is prescribed using observation-based SIC from COBE-SST2 (Fig. 14a–c,g–i). Figure 14 also includes the SIC estimated, as in the NH, using the COBE-SST2 coefficients and SST [Eq. (28)]. The SIC estimated for the NW climate using the COBE-SST2 coefficients exhibits a broader extent of thin sea ice near the ice edge compared with observation-

based data. In August 1970, numerous ice-free "hole" structures appear along the sea ice margin (Fig. 14j). Such features are rarely seen in monthly observation-based analysis. Therefore, the estimation based on COBE-SST2 coefficients and SST is not applied in the SH.

Prescribing NW SIC in the SH using observation-based SIC does not contradict the spatial distributions of SST and SSS estimated under the NW climate. For SST, changes are small south of 60°S (Fig. 8a). The estimated NW SSS shows pronounced salinification in the Arctic Ocean, whereas the increase in salinity in the Southern Ocean is considerably smaller than that in the Arctic Ocean (Fig. 8e). The enhanced salinity in polar regions is likely associated with sea-ice formation in the NW climate. The weaker salinification in the Southern Ocean compared with the Arctic Ocean in CMIP-based estimates suggests that sea-ice changes driven by global warming are smaller in the Southern Ocean than in the Arctic Ocean. Nevertheless, warming-induced changes in Antarctic sea ice may still play a role. Accordingly, the estimation method for the Antarctic SIC remains an issue in future work.

Future climate

For the future SIC, we focus on the year 2050 under SSP2-4.5. In the NH, the SIC is determined based on the change in the SIA in each model (Fig. 3e), and adjusted to be consistent with the SST (see the Method section). Future SST after 2021 is generated by shifting the phase of internal variability from 1961, 1971, 1981, 1991, 2001, and 2011 (see the Method section), so that the SIC differs not only among models but also depending on the phase of internal variability. Figures 15 and 16 show the February and August SICs in 2050 under SSP2-4.5 for each model, respectively. The differences among the panels of the same model correspond to the different phases of internal variability, with the internal variability years aligned to 1970, 1990, and 2010 in 2050.

The ratio of the February 2050 SIA to the present climate ranges from a minimum of 86% in IPSL-CM6A-LR to a maximum of 97% in CNRM-CM6-1, indicating a relatively small spread across models (Fig. 3e). CESM2 and CNRM-CM6-1 exhibit relatively larger sea ice extent, but inter-model differences remain modest although they are still larger than the differences associated with internal variability (Fig. 15).

In contrast, the spread is larger in August than in February. The August 2050 SIA relative to that in the present climate ranges from a minimum of 14% for IPSL-CM6A-LR to a maximum of 75% for CNRM-CM6-1, with differences reaching about 61% (Fig. 3e). Indeed, SIC tends to

be considerably lower for IPSL-CM6A-LR and higher for CNRM-CM6-1 (Fig. 16). Although the impact of internal variability is smaller than that of inter-model differences, the effect is more pronounced in August than in February.

In the SH, we evaluate the change in SIA relative to 1995–2014 (Fig. 3f), and apply this change to retreat the observation-based SIC from the present climate (1995–2014) as described in the Method section. For example, the February SIA of MPI-ESM1-2-LR in 2050 is 63% relative to that in the present climate (Fig. 3f). Accordingly, the retreated SIC distribution similar to Fig. 3k which is 60% relative to the observation-based climatology in 1995–2014 (Fig. 3i) is used to represent the February SIC of MPI-ESM1-2-LR in 2050.

Data Availability

The data is available at `https://climate.mri-jma.go.jp/pub/archives/Ushijima-et-al_Upper_Ocean_Data`, and metadata, documentation, and citation information for the dataset are archived through Zenodo[65].

Code Availability

The code used to construct the data and produce the figures is available at `https://github.com/usijimay/TSECOceanData`.

Funding

This work was supported by MEXT-Program for the advanced studies of climate change projection (SENTAN) Grant Number JPMXD0722680734.

Table 1: CMIP6 coupled models used in this study with corresponding abbreviations, ensemble members, coupled model components, and references.

Model Name	abbr.	Members	Atmospheric Model	Ocean Model	reference
ACCESS-CM2	AC	5	UM GA7.1	MOM5	Bi et al.[69]
CESM2	CE	4	CAM6	POP2	Danabasoglu et al.[70]
CNRM-CM6-1	CN	6	ARPEGE-Climat v6.3	NEMO v3.6	Voldoire et al.[71]
CanESM5	Ca	10	CanAM5	NEMO v3.4	Swart et al.[72]
IPSL-CM6A-LR	IP	6	LMDZ6A-LR	NEMO v3.6	Boucher et al.[73]
MIROC6	MI	30	MIROC6 AGCM	COCO v4.0	Tatebe et al.[74]
MPI-ESM1-2-LR	MP	30	ECHAM6.3	MPIOM1.6	Mauritsen et al.[75]
MRI-ESM2-0	MR	5	MRI-AGCM3.5	MRI.COMv4	Yukimoto et al.[76]
UKESM1-0-LL	UK	5	UM GA7.1	NEMO v3.6	Sellar et al.[77]

Table 2: The explained variance and S/N ratio of each EOF mode in the present climate, with annual means and standard deviations (representing seasonal variations) calculated from the monthly values. The model names are expressed in abbreviations in Table 1.

	Explained Variance (%)			S/N ratio		
Model	1st mode	2nd mode	3rd mode	1st mode ($\times 10^2$)	2nd mode	3rd mode
AC	85 ± 1.1	6.8 ± 1.0	1.5 ± 0.40	2.3 ± 0.18	26 ± 6.2	3.4 ± 1.0
CE	77 ± 0.44	13 ± 0.42	3.0 ± 0.25	0.82 ± 0.024	13 ± 0.42	1.7 ± 0.23
CN	88 ± 1.1	3.2 ± 0.18	2.4 ± 0.37	1.1 ± 0.11	1.5 ± 0.36	5.8 ± 1.2
Ca	93 ± 0.60	4.5 ± 0.78	0.67 ± 0.13	13 ± 0.97	70 ± 18	3.8 ± 0.68
IP	92 ± 1.5	2.2 ± 0.28	1.2 ± 0.46	2.2 ± 0.39	5.5 ± 1.1	4.4 ± 1.5
MI	91 ± 0.34	6.3 ± 0.68	0.72 ± 0.20	11 ± 1.3	65 ± 14	11 ± 2.5
MP	96 ± 0.34	2.1 ± 0.16	0.55 ± 0.11	17 ± 1.2	13 ± 2.0	6.8 ± 1.2
MR	80 ± 0.59	12 ± 1.3	1.9 ± 0.52	2.2 ± 0.17	34 ± 6.2	4.2 ± 1.2
UK	82 ± 1.1	10 ± 1.1	2.1 ± 0.54	1.0 ± 0.10	37 ± 8.0	1.8 ± 0.61

Table 3: Same as Table 2, but for the future climate with SSP1-2.6 scenario.

	Explained Variance (%)			S/N ratio		
Model	1st mode	2nd mode	3rd mode	1st mode ($\times 10^2$)	2nd mode ($\times 10$)	3rd mode
CE	94 ± 0.84	3.3 ± 0.60	0.59 ± 0.069	4.2 ± 0.056	3.1 ± 0.60	0.99 ± 0.25
CN	92 ± 1.0	5.0 ± 0.88	1.2 ± 0.15	9.0 ± 0.51	4.7 ± 1.1	4.3 ± 0.89
IP	95 ± 0.88	2.3 ± 0.17	0.71 ± 0.20	2.9 ± 0.67	1.7 ± 0.34	3.0 ± 0.67
MI	93 ± 1.1	6.1 ± 0.89	0.51 ± 0.095	39 ± 7.6	63 ± 6.3	26 ± 2.6
MP	95 ± 0.91	2.8 ± 0.43	0.94 ± 0.26	13 ± 1.2	2.0 ± 0.20	21 ± 5.0
MR	88 ± 0.54	8.9 ± 0.21	1.4 ± 0.28	7.4 ± 0.38	9.6 ± 0.41	13 ± 2.8

Table 4: Same as Table 3, but for SSP2-4.5.

	Explained Variance (%)			S/N ratio		
Model	1st mode	2nd mode	3rd mode	1st mode ($\times 10^2$)	2nd mode ($\times 10$)	3rd mode
CE	97 ± 0.29	1.3 ± 0.16	0.45 ± 0.073	7.3 ± 0.12	4.4 ± 0.57	3.0 ± 0.63
CN	96 ± 0.39	2.1 ± 0.23	0.52 ± 0.083	14 ± 1.1	1.7 ± 0.29	9.9 ± 1.7
IP	98 ± 0.28	0.73 ± 0.19	0.29 ± 0.035	8.5 ± 1.7	3.3 ± 1.4	11 ± 1.5
MI	98 ± 0.28	1.7 ± 0.19	0.40 ± 0.48	76 ± 13	61 ± 8.8	66 ± 12
MP	98 ± 0.36	1.1 ± 0.20	0.38 ± 0.093	42 ± 3.4	7.0 ± 0.97	17 ± 3.3
MR	95 ± 0.65	2.7 ± 0.31	0.94 ± 0.22	15 ± 0.88	5.9 ± 0.47	29 ± 5.9

Table 5: Same as Table 3, but for SSP5-8.5.

	Explained Variance (%)			S/N ratio		
Model	1st mode	2nd mode	3rd mode	1st mode ($\times 10^2$)	2nd mode ($\times 10$)	3rd mode
AC	99 ± 0.23	0.63 ± 0.11	0.13 ± 0.030	4.9 ± 0.47	11 ± 1.6	9.8 ± 1.8
CE	99 ± 0.16	0.83 ± 0.097	0.23 ± 0.035	2.2 ± 0.061	5.8 ± 0.61	5.9 ± 0.90
CN	98 ± 0.26	1.2 ± 0.20	0.21 ± 0.041	3.7 ± 0.39	3.3 ± 0.86	17 ± 4.3
Ca	99 ± 0.13	0.79 ± 0.093	0.18 ± 0.026	19 ± 2.2	38 ± 5.3	51 ± 5.6
IP	99 ± 0.40	0.71 ± 0.34	0.15 ± 0.033	3.0 ± 0.57	32 ± 18	14 ± 5.0
MI	99 ± 0.20	0.99 ± 0.19	0.28 ± 0.041	21 ± 3.4	70 ± 25	310 ± 62
MP	99 ± 0.16	0.76 ± 0.12	0.14 ± 0.019	15 ± 1.2	38 ± 4.4	42 ± 3.3
MR	98 ± 0.39	1.6 ± 0.23	0.37 ± 0.085	3.8 ± 0.29	9.4 ± 0.85	46 ± 8.0
UK	99 ± 0.29	0.88 ± 0.22	0.21 ± 0.046	3.1 ± 0.47	25 ± 6.4	26 ± 3.3

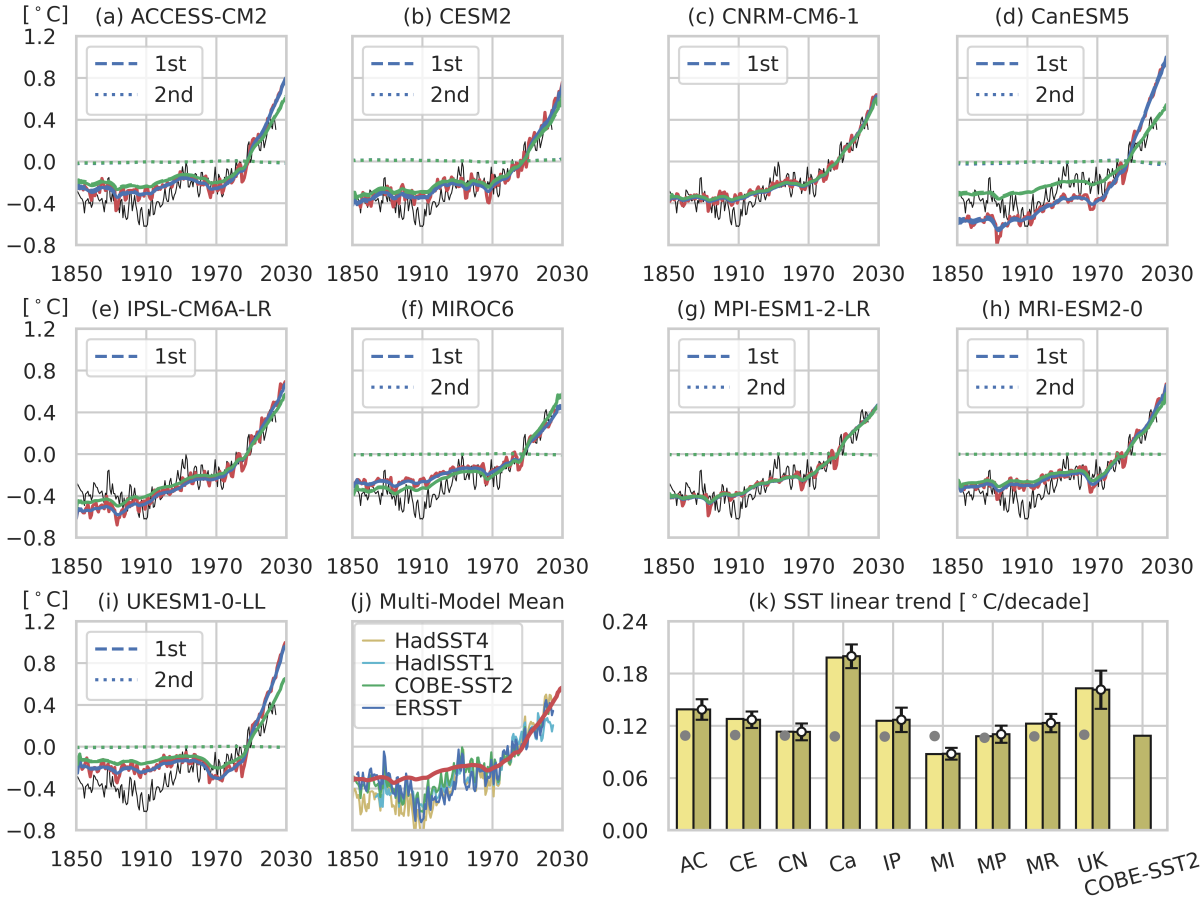


Figure 1: (a)–(i) Annual GMSST time series for each model (red). The solid blue line shows the SST from the extracted forced component (for CNRM-CM6-1 and IPSL-CM6A-LR, the first EOF mode; for other models, the sum of the first and second EOF modes). The blue dashed and dotted lines indicate the annual mean SST from the first and second EOF modes, respectively. The green line shows the SST after sensitivity adjustment of each EOF mode. Thin black lines represent COBE-SST2 GMSST. (j) Time series of the multi-model mean of the sensitivity-adjusted forced GMSST change (red line). Other colors indicate differences among observation-based datasets. (k) Linear trends of the annual mean GMSST for 1961–2020 (°C/decade). The model names are expressed in abbreviations in Table 1. Khaki bars show the ensemble mean of each model, with error bars representing standard deviation. Yellow bars indicate the warming trend of the extracted forced component. COBE-SST2 trends are also shown as khaki bars and gray circles.

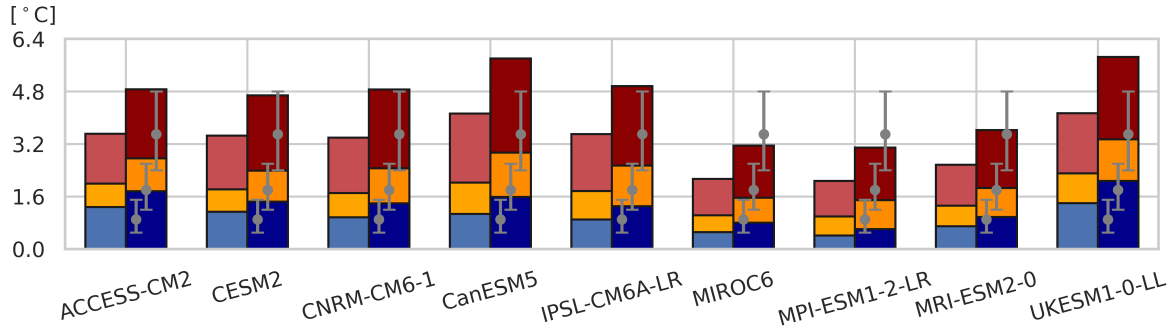


Figure 2: Differences in annual mean GMSST (left) and GMSAT (right) between 1995–2014 and 2081–2100 for each model. Colors indicate scenarios (blue: SSP1-2.6, orange: SSP2-4.5, red: SSP5-8.5). Gray circles and error bars show the central estimates of the assessed warming and their very likely (5—95%) ranges, respectively, reported in Table 4.5 of the IPCC AR6 WG1 Full Report[51].

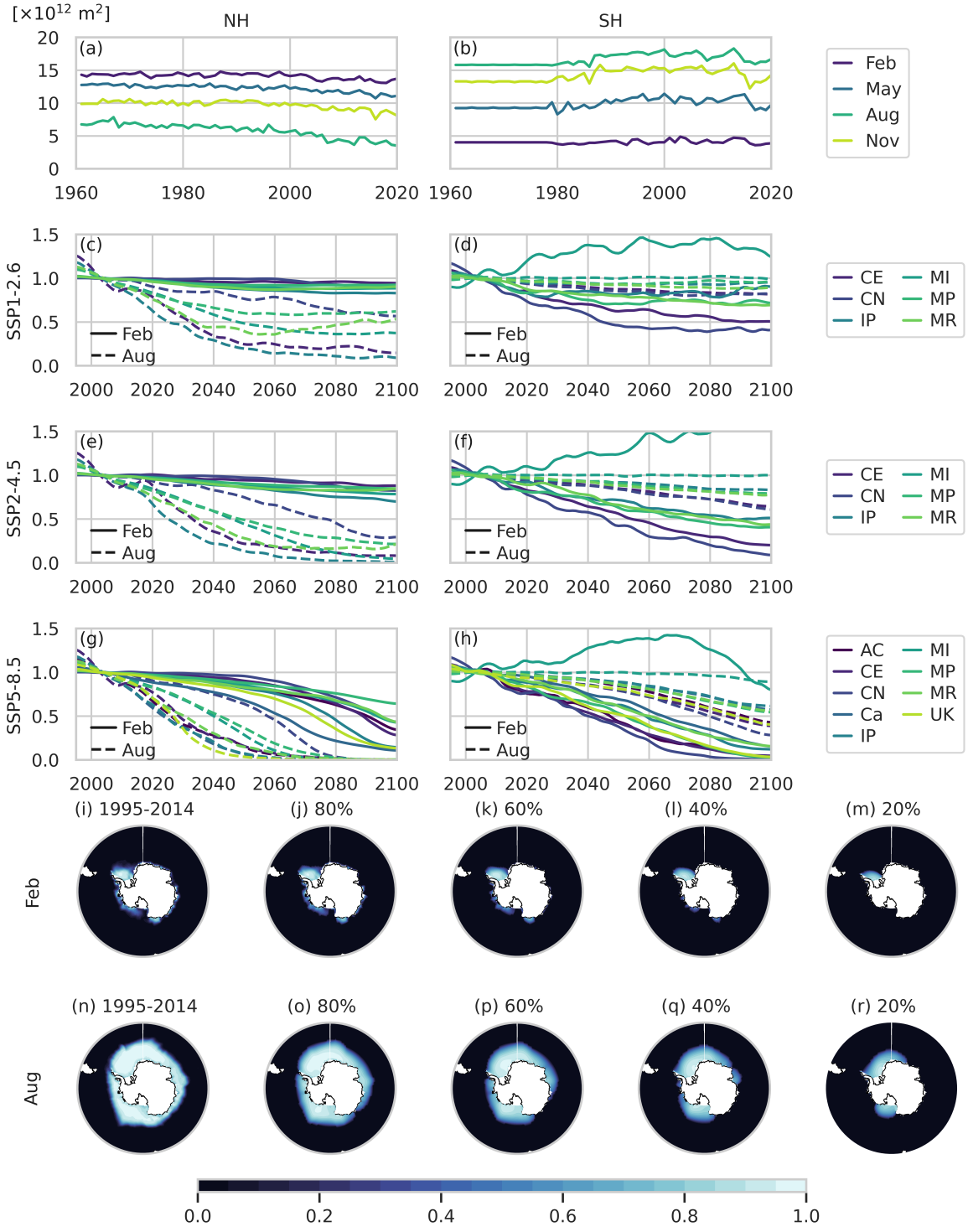


Figure 3: (a), (b) Time series of monthly mean SIAs from COBE-SST2 in the (a) NH and (b) SH. (c)–(h) Time series of low-pass filtered monthly SIAs relative to the 1995–2014 average for each model in the (c), (e), (g) NH and (d), (f), (h) SH under (c), (d) SSP1-2.6, (e), (f) SSP2-4.5, and (g), (h) SSP5-8.5 scenarios. Model names are given as abbreviations in Table 1. The cutoff period of the filter is 10 years. Solid and dashed lines denote February and August, respectively. (i)–(r) SH SIC in (i)–(m) February and (n)–(r) August. Climatological means are shown for (i), (n) 1995–2014 from COBE-SST2. SIC distributions obtained by retreating sea ice to (j), (o) 80%, (k), (p) 60%, (l), (q) 40%, and (m), (r) 20% of the 1995–2014 monthly climatological SIA from COBE-SST2 are shown.

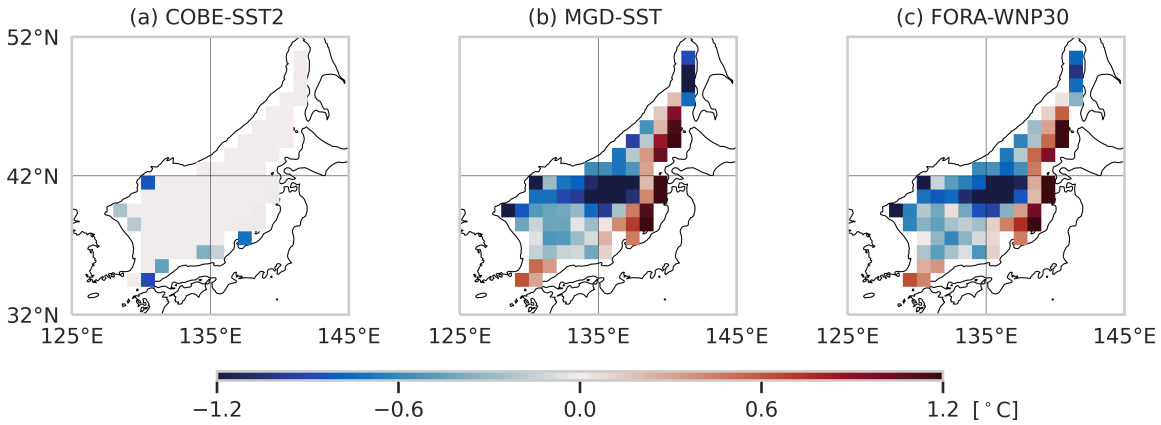


Figure 4: Climatological SST anomalies of (a) COBE-SST2, (b) MGDSST, and (c) FORA-WNP30 relative to the SST climatology of Ishii et al.[47] for February in 1982–2016 in the Japan Sea.

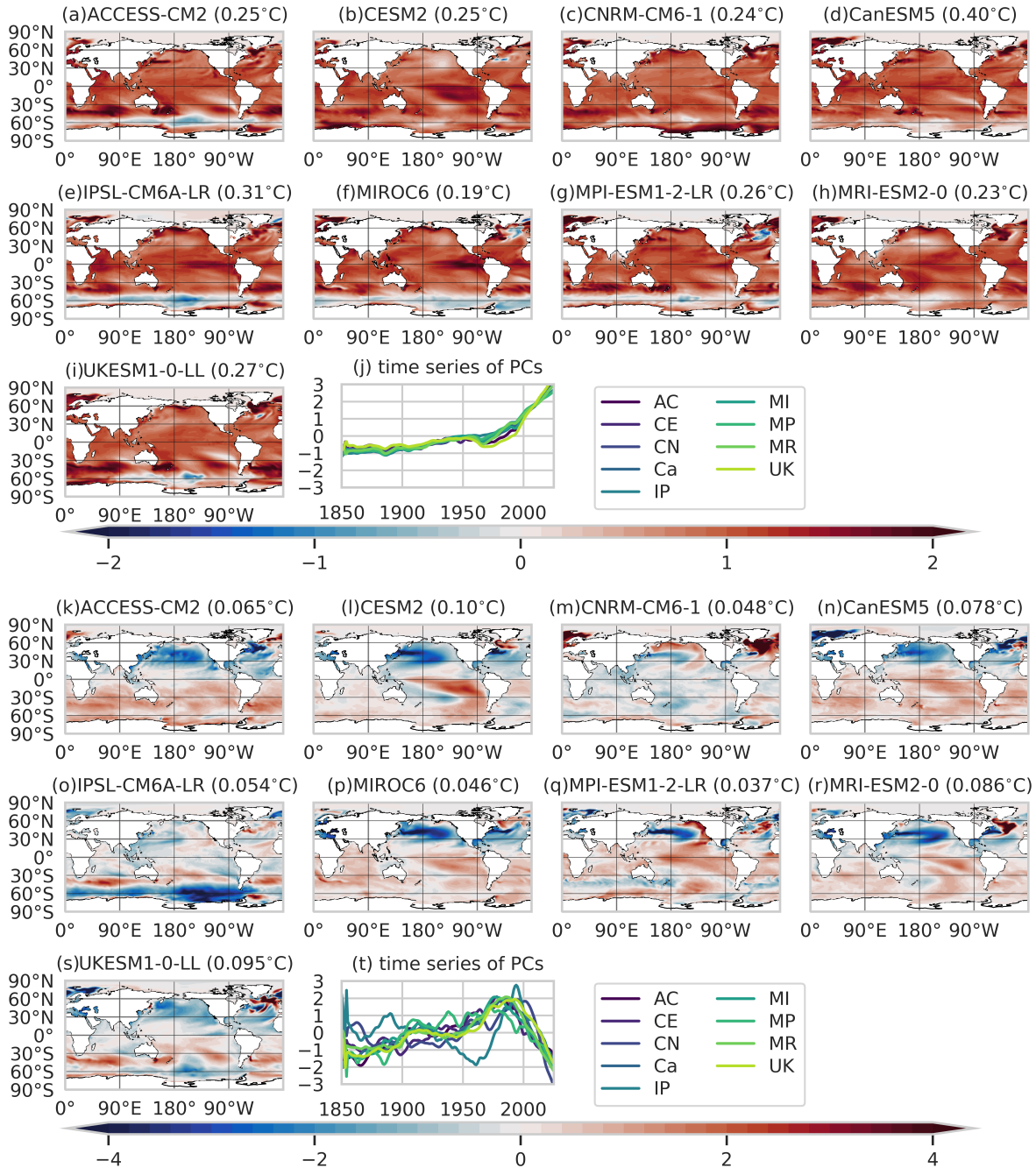


Figure 5: Normalized spatial patterns of the (a)–(i) first (x_1) and (k)–(s) second (x_2) EOF modes of February SST and extended time series of the corresponding normalized PCs of the (j) first (t'_1) and (t) second (t'_2) modes from the historical and SSP2-4.5 simulations in 1850–2025. The model names in j and t are expressed in abbreviations in Table 1. Normalization is performed using the square root of the horizontally averaged variance for each mode (values shown next to the model names).

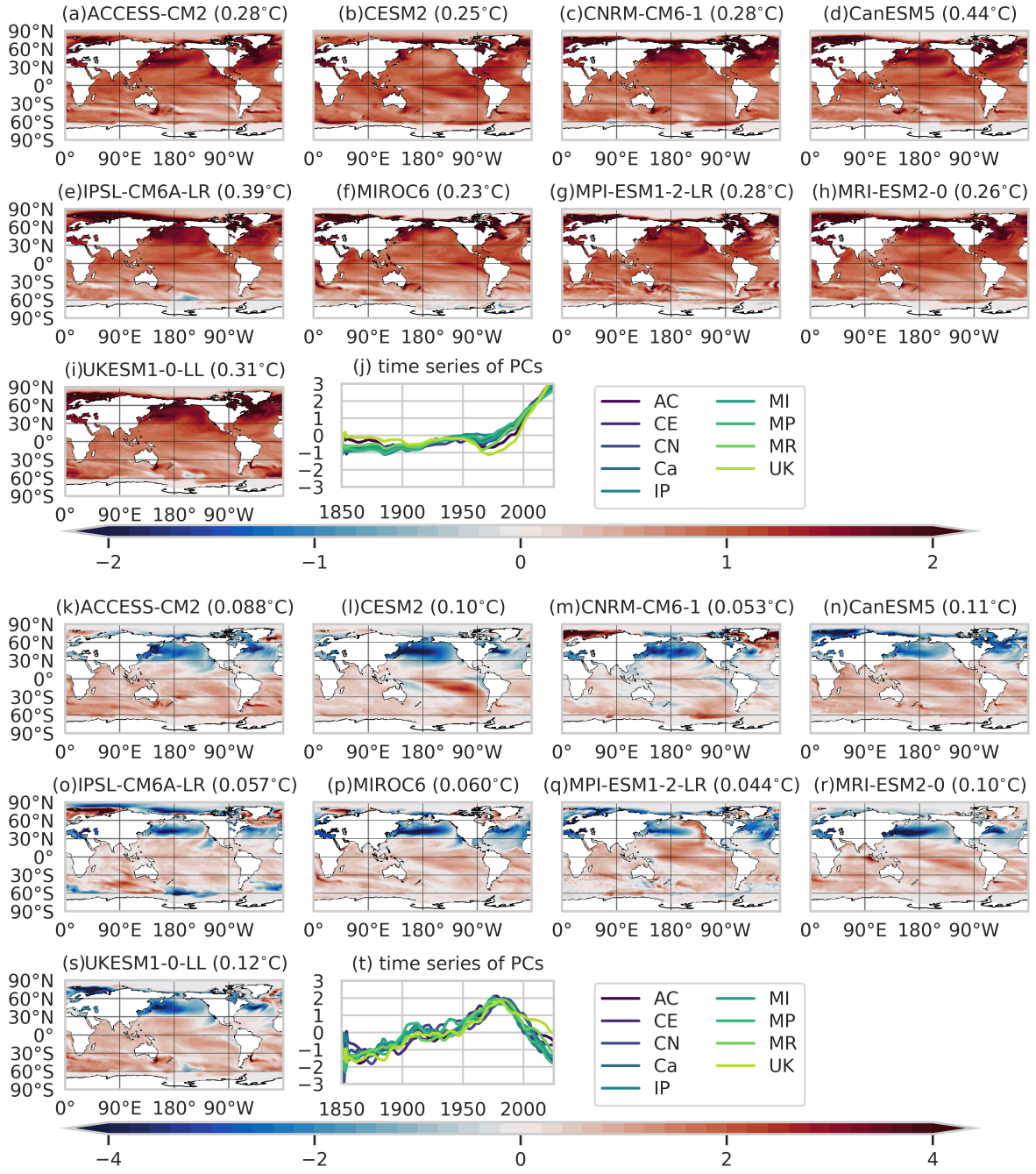


Figure 6: Same as Fig. 5 but for August.

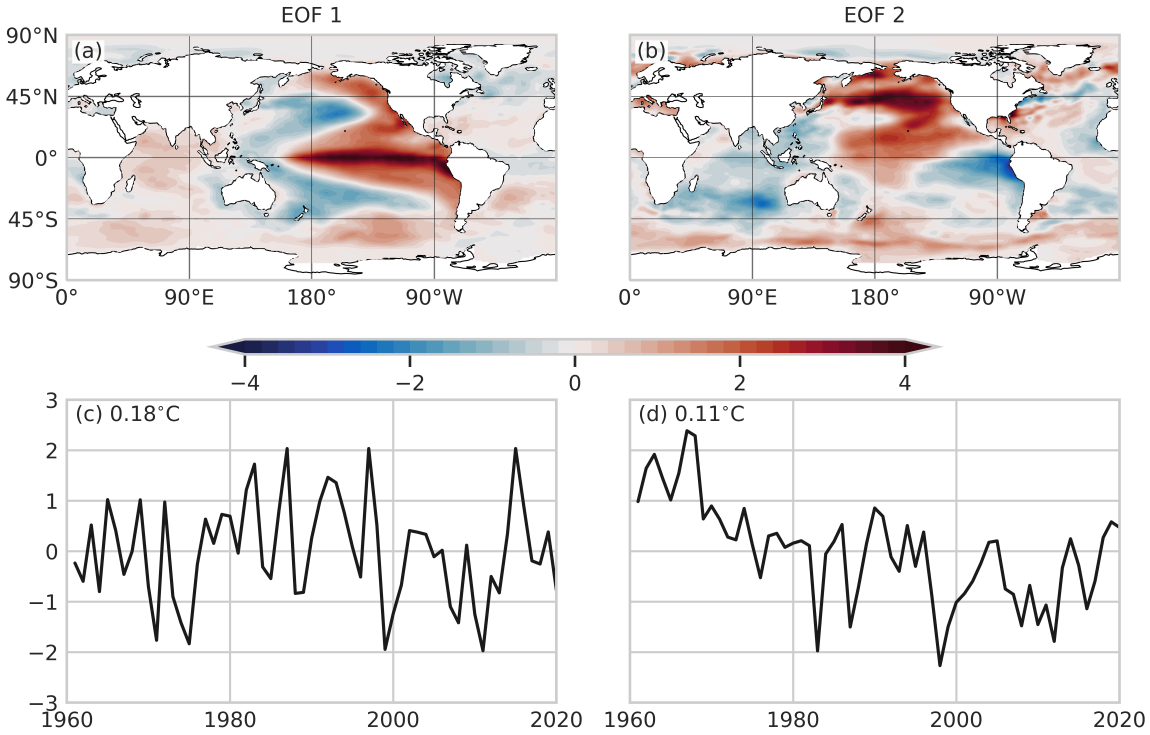


Figure 7: Normalized spatial patterns of the (a) first and (b) second EOF modes and time series of the PCs of (c) first and (d) second modes of the internal variability of the annual mean SST. Normalization is performed using the square root of the horizontally averaged variance for each mode (values shown in the PC panels).

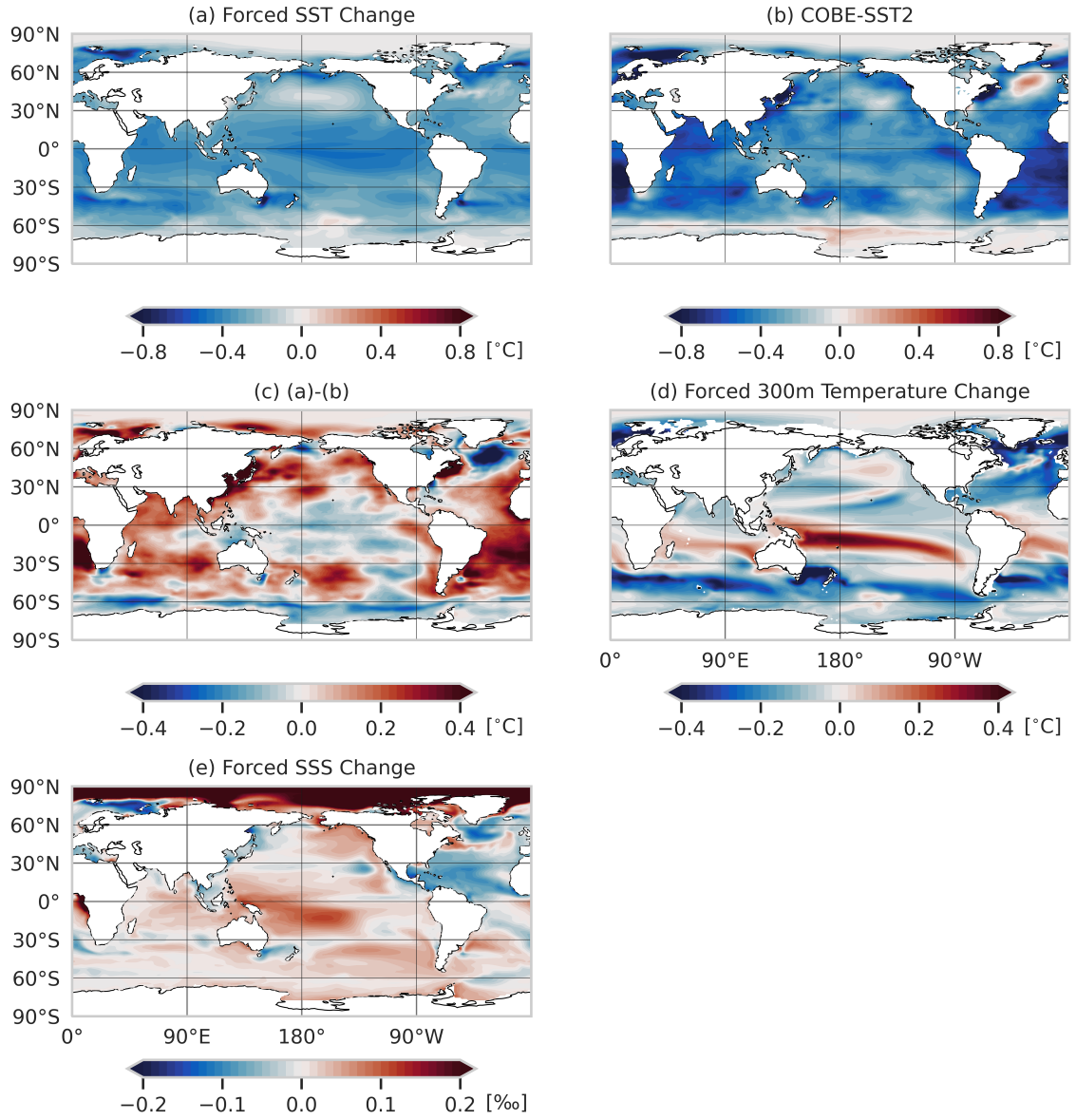


Figure 8: Differences between 1850–1899 and 1961–2020 in (a) the annual-mean externally forced SST change [$\theta_f(z = 0)$ in Eq. (17)], (b) annual-mean SST from COBE-SST2, and (c) their difference. Same as (a), but for (d) temperature at 300 m [$\theta_f(z = 300\text{ m})$ in Eq. (17)] and (e) SSS [$S_f(z = 0)$ in Eq. (18)].

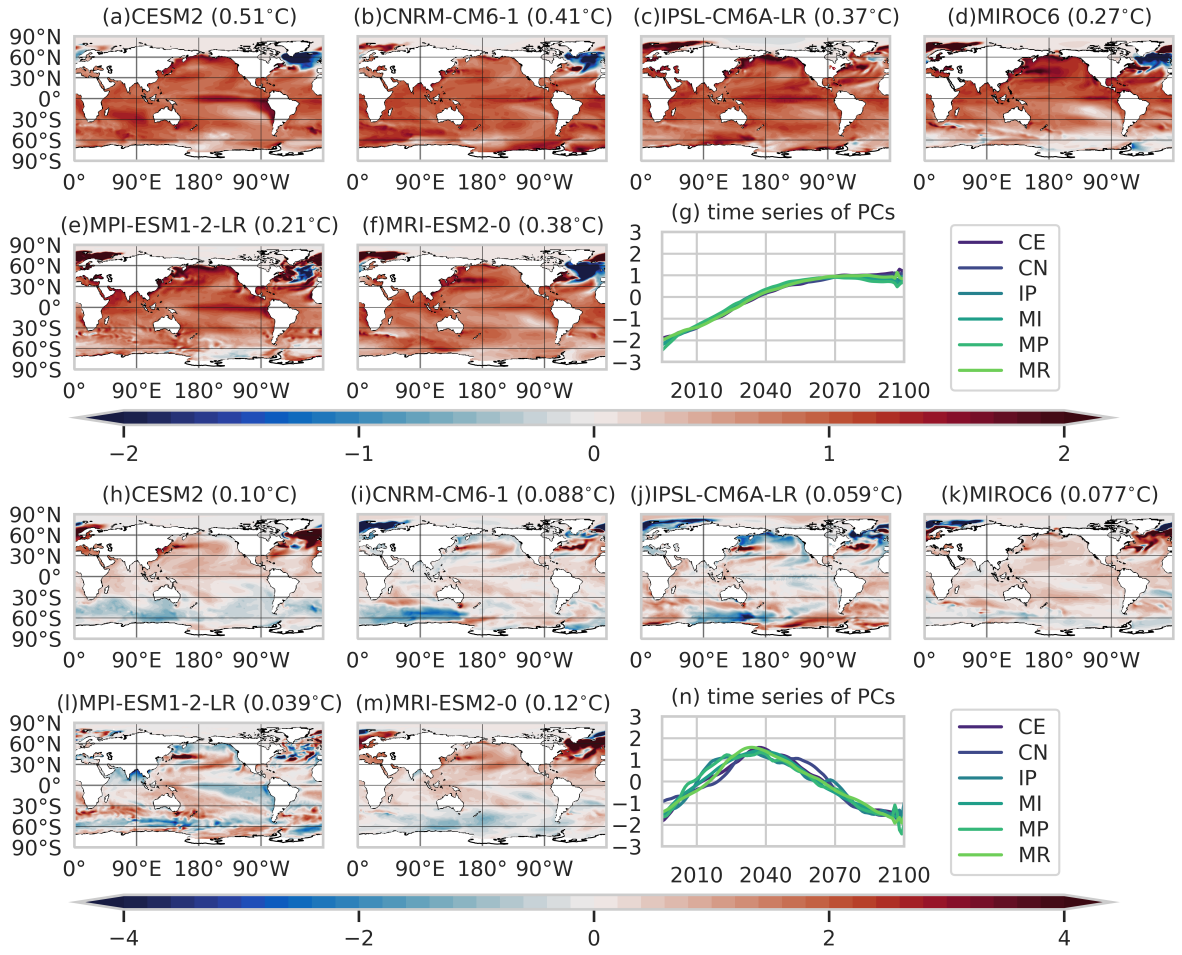


Figure 9: Same as Fig. 5, but for (a)–(f) first and (h)–(m) second EOF modes and PCs of the (g) first and (n) second modes from the historical and SSP1-2.6 simulations in 1995–2100.

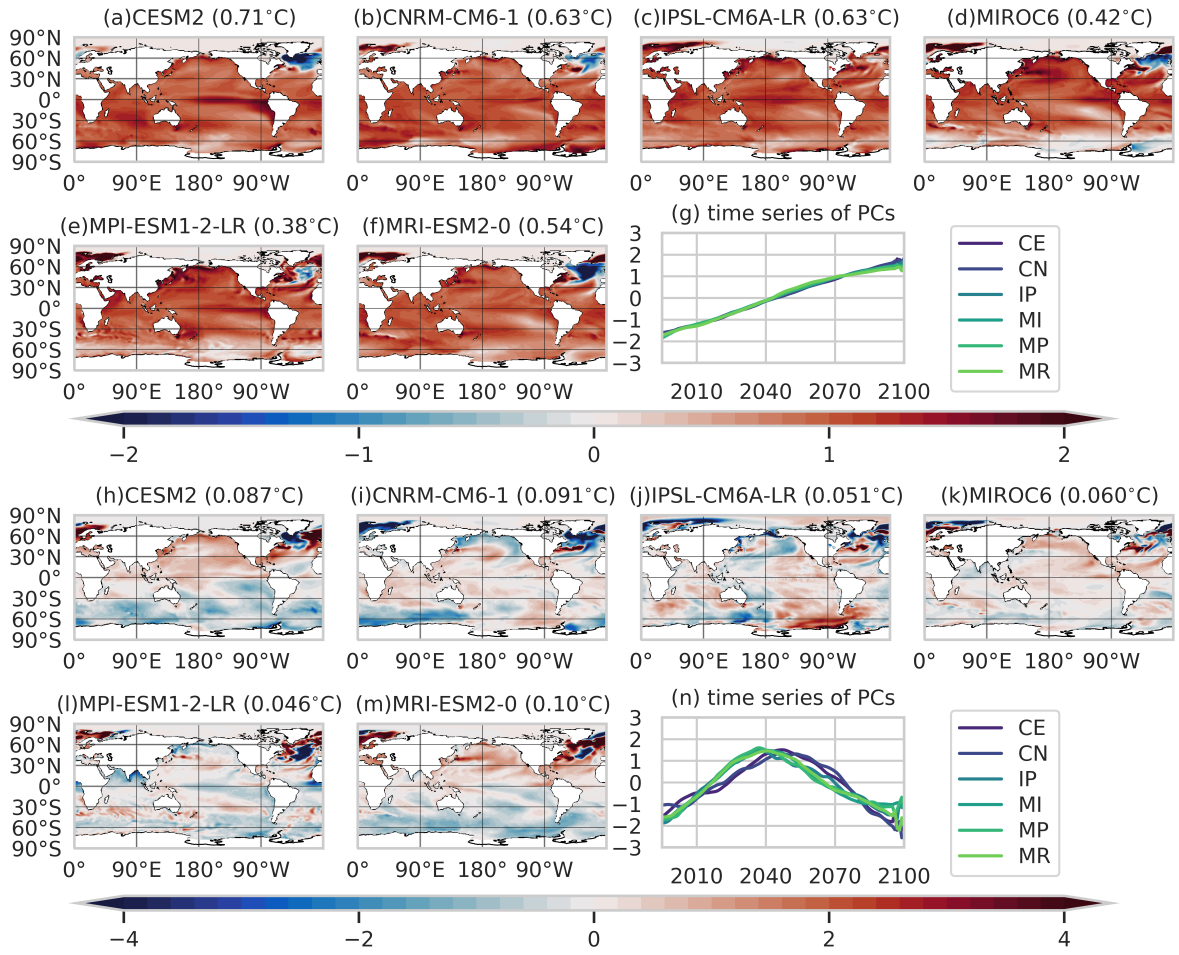


Figure 10: Same as Fig. 9, but for the historical and SSP2-4.5 simulations

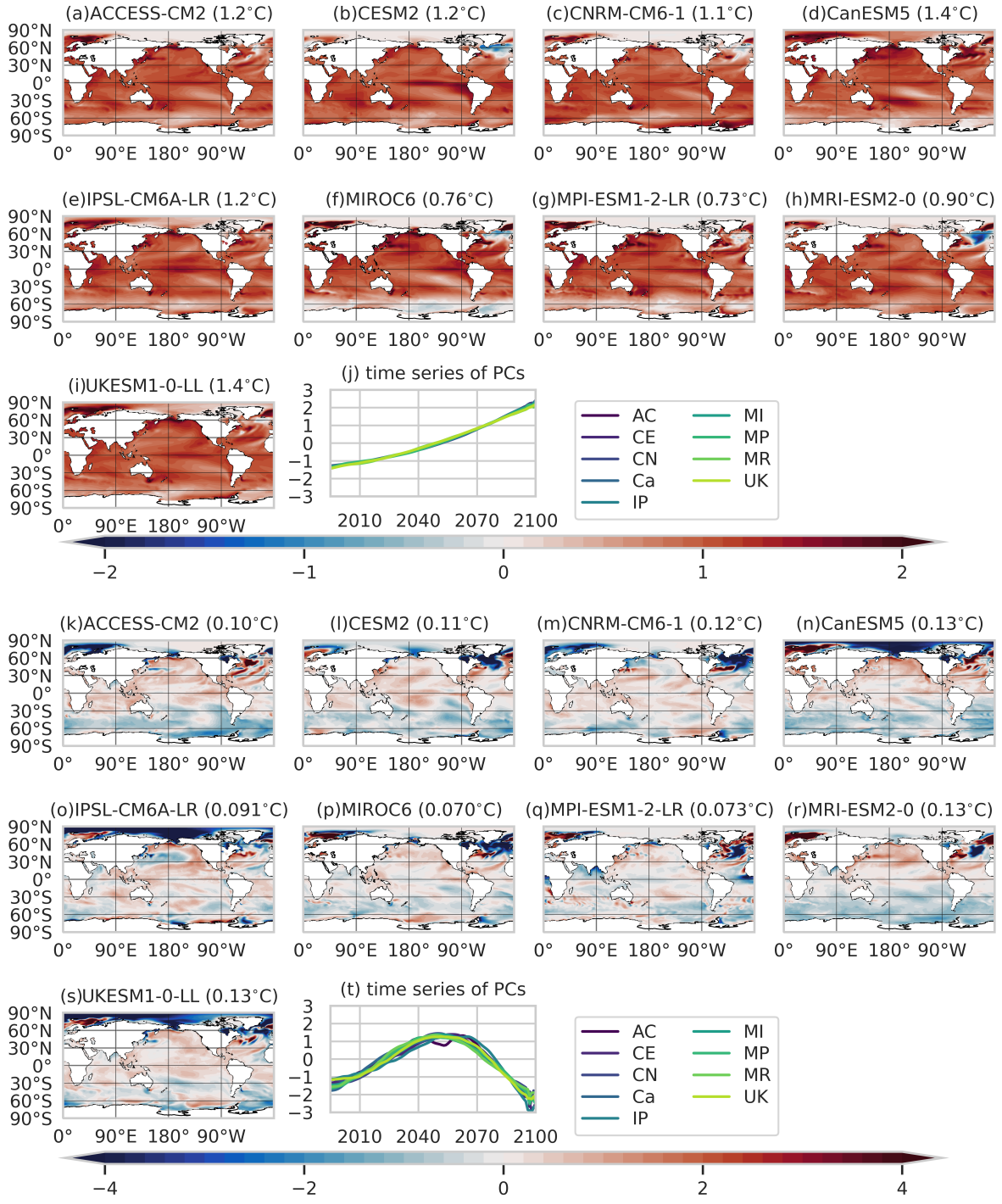


Figure 11: Same as Fig. 5, but for the historical and SSP5-8.5 simulations in 1995–2100.

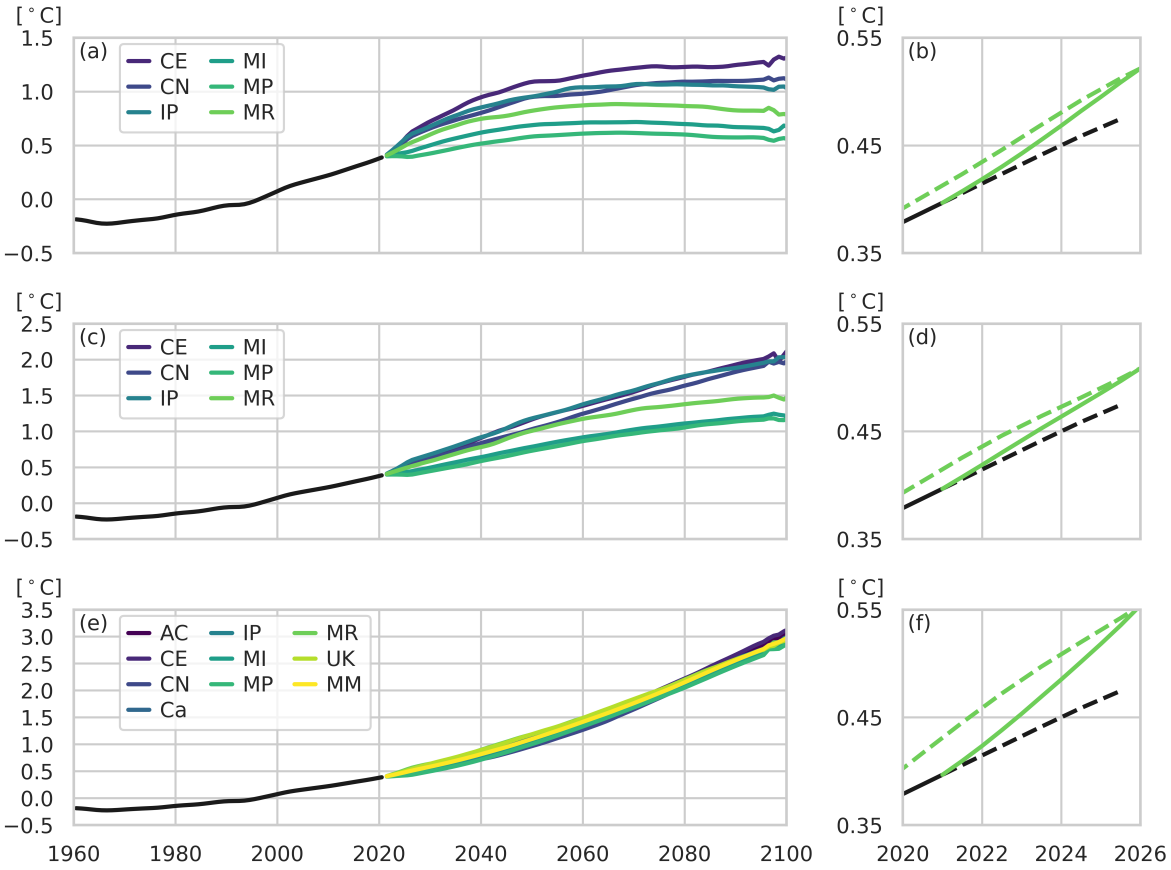


Figure 12: Time series of the forced GMSST changes under (a), (b) SSP1-2.6, (c), (d) SSP2-4.5, and (e), (f) SSP5-8.5 scenarios. The dashed lines colored in black and light green in (b), (d), and (f) show the forced changes derived from the multi-model mean for 1855–2025 and the MRI-ESM2-0 data for 1995–2095, respectively, while the light green solid line is the weighted average of the two estimates in Eq. (27).

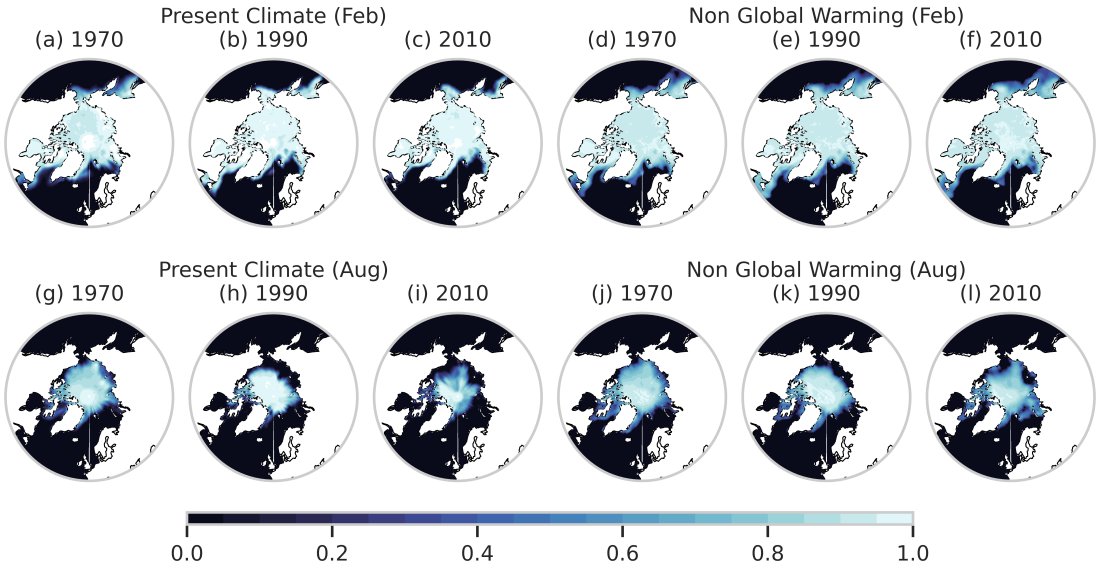


Figure 13: NH SIC in (a)–(f) February and (g)–(l) August. Panels (a)–(c) and (g)–(i) show the present climate for 1970, 1990, and 2010, respectively, while panels (d)–(f) and (j)–(l) show the NW climate for the corresponding internal variability years.

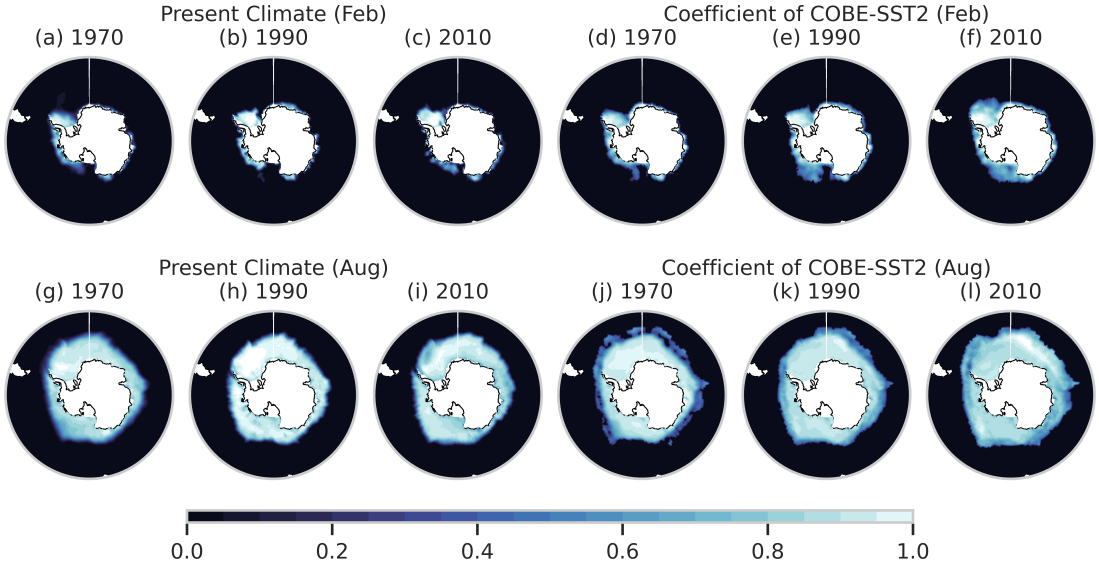


Figure 14: SH SIC in (a)–(f) February and (g)–(l) August. Panels (a)–(c) and (g)–(i) show the present climate for 1970, 1990, and 2010, respectively, while panels (d)–(f) and (j)–(l) show the NW climate for the corresponding internal variability years, estimated using the COBE-SST2 coefficients and SST [Eq. (28)]. [Note that, although panels (d)–(f) and (j)–(l) show the NW SIC estimated from the COBE-SST2 coefficients and SST, the NW SIC used in our dataset for the internal variability years (1970, 1990, and 2010) is prescribed from the corresponding present-climate SIC.]

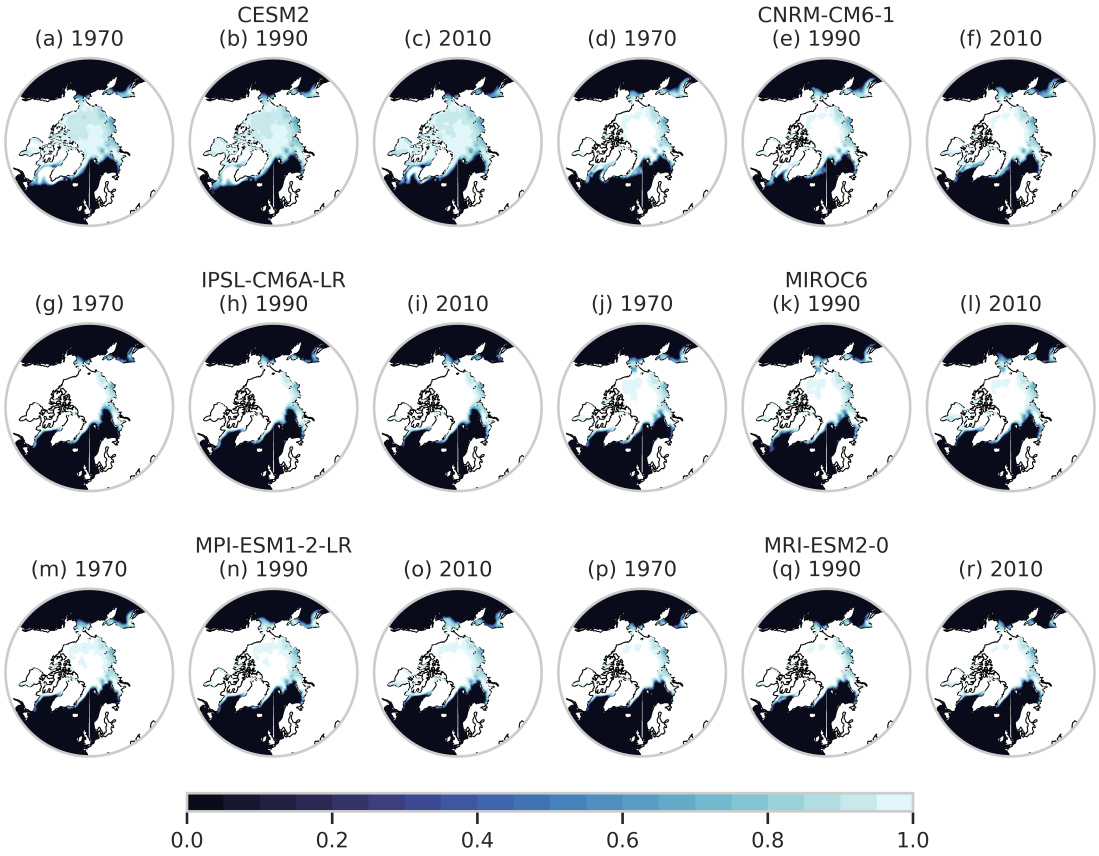


Figure 15: Evaluated SIC for each model in February 2050 under the SSP2-4.5 scenario in the year of the internal variability of (a), (d), (g), (j), (m), (p) 1970, (b), (e), (h), (k), (n), (q) 1990, and (c), (f), (i), (l), (o), (r) 2010.

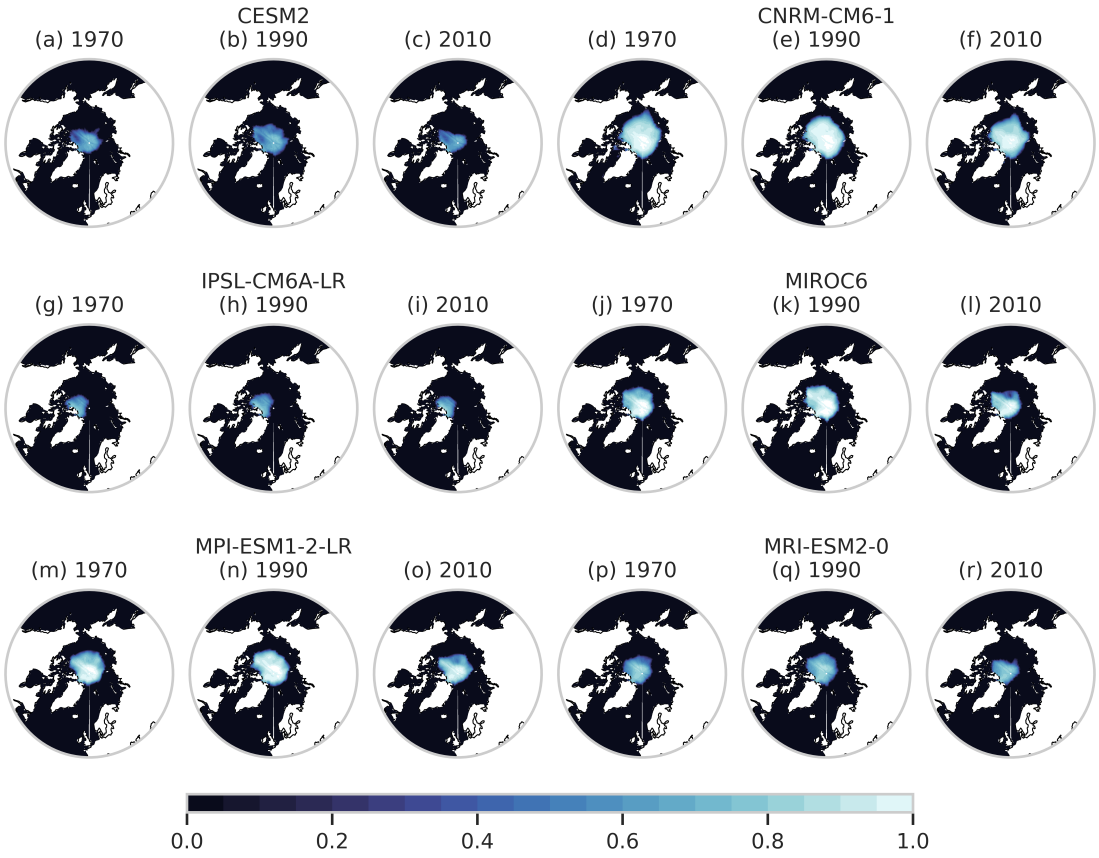


Figure 16: Same as Fig. 15, but for August.

References

[1] Gen Li and Shang-Ping Xie. Origins of tropical-wide SST biases in CMIP multi-model ensembles. *Geophys. Res. Lett.*, 39(22), 2012. https://doi.org/10.1029/2012GL053777.

[2] Yuchao Zhu, Rong-Hua Zhang, and Jichang Sun. North Pacific Upper-Ocean Cold Temperature Biases in CMIP6 Simulations and the Tole of Regional Vertical Mixing. *J. Clim.*, 33(17):7523–7538, 2020. https://doi.org/10.1175/JCLI-D-19-0654.1.

[3] Qibei Zhang, Bo Liu, Shuanglin Li, and Tianjun Zhou. Understanding Models' Global Sea Surface Temperature Bias in Mean State: From CMIP5 to CMIP6. *Geophys. Res. Lett.*, 50 (4):e2022GL100888, 2023. https://doi.org/10.1029/2022GL100888.

[4] Liping Zhang and Chuanhu Zhao. Processes and mechanisms for the model SST biases in the North Atlantic and North Pacific: A link with the Atlantic meridional overturning circulation. *J. Adv. Model. Earth Syst.*, 7(2):739–758, 2015. https://doi.org/10.1002/2014MS000415.

[5] Rajat Joshi and Rong Zhang. Impacts of the North Atlantic biases on the upper troposphere/lower stratosphere over the extratropical North Pacific. *npj Clim. Atmos. Sci.*, 6 (1):151, 2023. https://doi.org/10.1038/s41612-023-00482-4.

[6] Xuehong Zhang, Wuyin Lin, and Minghua Zhang. Toward understanding the double Intertropical Convergence Zone pathology in coupled ocean-atmosphere general circulation models. *J. Geophys. Res. Atmos.*, 112(D12), 2007. https://doi.org/10.1029/2006JD007878.

[7] Jing Ma, Haiming Xu, and Pengfei Lin. Meridional position biases of East Asian subtropical jet stream in CMIP5 models and their relationship with ocean model resolutions. *Int. J. Climatol.*, 35(13), 2015. https://doi.org/10.1002/joc.4256.

[8] Akio Kitoh, Tomoaki Ose, and Izuru Takayabu. Dynamical Downscaling for Climate Projection with High-Resolution MRI-AGCM-RCM. *J. Meteorol. Soc. Jpn.*, 94(0):1–16, 2016. https://doi.org/10.2151/jmsj.2015-022.

[9] Baoqiang Xiang, Ming Zhao, Isaac M Held, and Jean-Christophe Golaz. Predicting the severity of spurious "double ITCZ" problem in CMIP5 coupled models from AMIP

simulations. *Geophys. Res. Lett.*, 44(3):1520–1527, 2017. https://doi.org/10.1002/2016GL071992.

[10] Yusuke Ushijima, Ryo Mizuta, Shion Sekizawa, and Hiroyuki Tsujino. Assessing the Impact of Sea Surface Temperature Biases in CMIP6 Coupled Models on the North Pacific Westerly Jet. *Geophys. Res. Lett.*, 53:e2026GL124012, 2026. https://doi.org/10.1029/2026GL124012.

[11] Pardeep Pall, Tolu Aina, Dáithí A Stone, Peter A Stott, Toru Nozawa, Arno GJ Hilberts, Dag Lohmann, and Myles R Allen. Anthropogenic greenhouse gas contribution to flood risk in England and Wales in autumn 2000. *Nature*, 470(7334):382–385, 2011. https://doi.org/10.1038/nature09762.

[12] Nikolaos Christidis, Peter A Stott, Adam A Scaife, Alberto Arribas, Gareth S Jones, Dan Copsey, Jeff R Knight, and Warren J Tennant. A New HadGEM3-A-Based System for Attribution of Weather- and Climate-Related Extreme Events. *J. Clim.*, 26(9):2756–2783, 2013. https://doi.org/10.1175/JCLI-D-12-00169.1.

[13] Hideo Shiogama, Masahiro Watanabe, Yukiko Imada, Masato Mori, Masayoshi Ishii, and Masahide Kimoto. An event attribution of the 2010 drought in the South Amazon region using the MIROC5 model. *Atmos. Sci. Lett.*, 14(3):170–175, 2013. https://doi.org/10.1002/asl2.435.

[14] Dáithí A Stone, Nikolaos Christidis, Chris Folland, Sarah Perkins-Kirkpatrick, Judith Perlwitz, Hideo Shiogama, Michael F Wehner, Piotr Wolski, Shreyas Cholia, Harinarayan Krishnan, et al. Experiment design of the International CLIVAR C20C+ Detection and Attribution project. *Weather Clim. Extrem.*, 24:100206, 2019. https://doi.org/10.1016/j.wace.2019.100206.

[15] Dáithí A Stone and Pardeep Pall. Benchmark estimate of the effect of anthropogenic emissions on the ocean surface. *Int. J. Climatol.*, 41(5):3010–3026, 2021. https://doi.org/10.1002/joc.7002.

[16] Hiroyuki Murakami, Yuqing Wang, Hiromasa Yoshimura, Ryo Mizuta, Masato Sugi, Eiki Shindo, Yukimasa Adachi, Seiji Yukimoto, Masahiro Hosaka, Shoji Kusunoki, et al. Future Changes in Tropical Cyclone Activity Projected by the New High-Resolution MRI-AGCM. *J. Clim.*, 25(9):3237–3260, 2012. https://doi.org/10.1175/JCLI-D-11-00415.1.

[17] Ryo Mizuta, Hiromasa Yoshimura, Hiroyuki Murakami, Mio Matsueda, Hirokazu Endo, Tomoaki Ose, Kenji Kamiguchi, Masahiro Hosaka, Masato Sugi, Seiji Yukimoto, et al. Climate Simulations Using MRI-AGCM3.2 with 20-km Grid. *J. Meteorol. Soc. Jpn.*, 90(0): 233–258, 2012. https://doi.org/10.2151/jmsj.2012-A12.

[18] Daniel Mitchell, Krishna AchutaRao, Myles Allen, Ingo Bethke, Urs Beyerle, Andrew Ciavarella, Piers M Forster, Jan Fuglestvedt, Nathan Gillett, Karsten Haustein, et al. Half a degree additional warming, prognosis and projected impacts (HAPPI): background and experimental design. *Geosci. Model Dev.*, 10(2):571–583, 2017. https://doi.org/10.5194/gmd-10-571-2017.

[19] Reindert J Haarsma, Malcolm J Roberts, Pier Luigi Vidale, Catherine A Senior, Alessio Bellucci, Qing Bao, Ping Chang, Susanna Corti, Neven S Fučkar, Virginie Guemas, et al. High Resolution Model Intercomparison Project (HighResMIP v1.0) for CMIP6. *Geosci. Model Dev.*, 9(11):4185–4208, 2016. https://doi.org/10.5194/gmd-9-4185-2016.

[20] Ryo Mizuta, Akihiko Murata, Masayoshi Ishii, Hideo Shiogama, Kenshi Hibino, Nobuhito Mori, Osamu Arakawa, Yukiko Imada, Kohei Yoshida, Toshinori Aoyagi, et al. Over 5,000 Years of Ensemble Future Climate Simulations by 60-km Global and 20-km Regional Atmospheric Models. *Bull. Am. Meteorol. Soc.*, 98(7):1383–1398, 2017. https://doi.org/10.1175/BAMS-D-16-0099.1.

[21] Nobuaki Kimura, Hirohide Kiri, and Iwao Kitagawa. The Impact of Multiple Typhoons on Severe Floods in the Mid-Latitude Region (Hokkaido). *Water*, 10(7):843, 2018. https://doi.org/10.3390/w10070843.

[22] Tomohiro Tanaka, Yasuto Tachikawa, Yutaka Ichikawa, and Kazuaki Yorozu. Flood risk curve development with probabilistic rainfall modelling and large ensemble climate simulation data: a case study for the Yodo River basin. *Hydrol. Res. Lett.*, 12(4):28–33, 2018. https://doi.org/10.3178/hrl.12.28.

[23] Nobuhito Mori, Tomoya Shimura, Kohei Yoshida, Ryo Mizuta, Yasuko Okada, Mikiko Fujita, Temur Khujanazarov, and Eiichi Nakakita. Future changes in extreme storm surges based on mega-ensemble projection using 60-km resolution atmospheric global circulation model. *Coast. Eng. J.*, 61(3):295–307, 2019. https://doi.org/10.1080/21664250.2019.1586290.

[24] Toshichika Iizumi, Hideo Shiogama, Yukiko Imada, Naota Hanasaki, Hiroki Takikawa, and Motoki Nishimori. Crop production losses associated with anthropogenic climate change for 1981–2010 compared with preindustrial levels. *Int. J. Climatol.*, 38(14):5405–5417, 2018. https://doi.org/10.1002/joc.5818.

[25] Sunmin Kim, Yasuto Tachikawa, and Eiichi Nakakita. Statistical Downscaling of AGCM60km Precipitation based on Spatial Correlation of AGCM20km Output. *Hydrol. Res. Lett.*, 11(1):58–64, 2017. https://doi.org/10.3178/hrl.11.58.

[26] Kuniyasu Sugawara, Masaru Inatsu, Seiji Shimoda, Keach Murakami, and Tomoyoshi Hirota. Risk Assessment and Possible Adaptation of Potato Production in Hokkaido to Climate Change Using a Large Number Ensemble Climate Dataset d4PDF. *SOLA*, 17:24–29, 2021. https://doi.org/10.2151/sola.2021-004.

[27] Masayoshi Ishii and Nobuhito Mori. d4PDF: large-ensemble and high-resolution climate simulations for global warming risk assessment. *Prog. Earth Planet. Sci.*, 7(1):1–22, 2020. https://doi.org/10.1186/s40645-020-00367-7.

[28] Hideo Shiogama, Yukiko Imada, Masato Mori, Ryo Mizuta, Dáithí Stone, Kohei Yoshida, Osamu Arakawa, Mikiko Ikeda, Chiharu Takahashi, Miki Arai, et al. Attributing Historical Changes in Probabilities of Record-Breaking Daily Temperature and Precipitation Extreme Events. *Sola*, 12:225–231, 2016. https://doi.org/10.2151/sola.2016-045.

[29] Yukiko Imada, Shuhei Maeda, Masahiro Watanabe, Hideo Shiogama, Ryo Mizuta, Masayoshi Ishii, and Masahide Kimoto. Recent Enhanced Seasonal Temperature Contrast in Japan from Large Ensemble High-Resolution Climate Simulations. *Atmosphere*, 8 (3):57, 2017. https://doi.org/10.3390/atmos8030057.

[30] Hiroaki Kawase, Tosiyuki Nakaegawa, Yukiko Imada, et al. Heavy Snowfall Has Already Been Enhanced by Anthropogenic Global Warming in Japan. *SOLA*, 20:167–176, 2024. https://doi.org/10.2151/sola.2024-023.

[31] H Kawase, Y Imada, H Sasaki, T Nakaegawa, A Murata, M Nosaka, and I Takayabu. Contribution of Historical Global Warming to Local-Scale Heavy Precipitation in Western Japan Estimated by Large Ensemble High-Resolution Simulations. *J. Geophys. Res. Atmos.*, 124(12):6093–6103, 2019. https://doi.org/10.1029/2018JD030155.

[32] Yukiko Imada, Hiroaki Kawase, Masahiro Watanabe, Miki Arai, Hideo Shiogama, and Izuru Takayabu. Advanced risk-based event attribution for heavy regional rainfall events. *npj climate and atmospheric science*, 3(1):37, 2020. https://doi.org/10.1038/s41612-020-00141-y.

[33] Daisuke Hatsuzuka, Hiroaki Kawase, and Yukiko Imada. Risk-Based Event Attribution Analysis of Anthropogenic Influence on the 2023 Baiu Extreme Rainfall in the Tohoku Region. *SOLA*, 21:175–182, 2025. https://doi.org/10.2151/sola.2025-022.

[34] Yukiko Imada, Masahiro Watanabe, Hiroaki Kawase, Hideo Shiogama, and Miki Arai. The July 2018 High Temperature Event in Japan Could Not Have Happened without Human-Induced Global Warming. *SOLA*, pages 15A–002, 2019. https://doi.org/10.2151/sola.15A-002.

[35] Rui Ito, Hiroaki Kawase, and Yukiko Imada. Regional Differences in Summertime Extremely High Temperature in Japan due to Global Warming. *J. Appl. Meteorol. Climatol.*, 61(10):1573–1587, 2022. https://doi.org/10.1175/JAMC-D-22-0062.1.

[36] M Fujita, R Mizuta, M Ishii, H Endo, T Sato, Y Okada, S Kawazoe, S Sugimoto, K Ishihara, and S Watanabe. Precipitation Changes in a Climate with 2-k Surface Warming From Large Ensemble Simulations Using 60-km Global and 20-km Regional Atmospheric Models. *Geophys. Res. Lett.*, 46(1):435–442, 2019. https://doi.org/10.1029/2018GL079885.

[37] Chao Li, Francis Zwiers, Xuebin Zhang, Guilong Li, Ying Sun, and Michael Wehner. Changes in Annual Extremes of Daily Temperature and Precipitation in CMIP6 Models. *J. Clim.*, 34(9):3441–3460, 2021. https://doi.org/10.1175/JCLI-D-19-1013.1.

[38] Ryo Mizuta, Masaya Nosaka, Toshiyuki Nakaegawa, Hirokazu Endo, Shoji Kusunoki, Akihiko Murata, and Izuru Takayabu. Extreme Precipitation in 150-year Continuous Simulations by 20-km and 60-km Atmospheric General Circulation Models with Dynamical Downscaling over Japan by a 20-km Regional Climate Model. *J. Meteorol. Soc. Jpn.*, 100 (3):523–532, 2022. https://doi.org/10.2151/jmsj.2022-026.

[39] Ed Hawkins, D Frame, L Harrington, Manoj Joshi, A King, M Rojas, and R Sutton. Observed Emergence of the Climate Change Signal: From the Familiar to the Unknown. *Geophys. Res. Lett.*, 47(6):e2019GL086259, 2020. https://doi.org/10.1029/2019GL086259.

[40] Ed Hawkins and Rowan Sutton. The Potential to Narrow Uncertainty in Regional Climate Predictions. *Bull. Am. Meteorol. Soc.*, 90(8):1095–1108, 2009. https://doi.org/10.1175/2009BAMS2607.1.

[41] Michiya Hayashi, Hideo Shiogama, Noriko N Ishizaki, and Yasutaka Wakazuki. Scenario Dependence of Future Precipitation Changes across Japan in CMIP6. *SOLA*, 20:207–216, 2024. https://doi.org/10.2151/sola.2024-028.

[42] Tomomichi Ogata, Ryo Mizuta, Yukimasa Adachi, Hiroyuki Murakami, and Tomoaki Ose. Effect of air-sea coupling on the frequency distribution of intense tropical cyclones over the northwestern Pacific. *Geophys. Res. Lett.*, 42(23):10–415, 2015. https://doi.org/10.1002/2015GL066774.

[43] Ryo Mizuta, Hirokazu Endo, Hideaki Kawai, Seiji Yukimoto, Kohei Yoshida, Hiromasa Yoshimura, Hiroyuki Tsujino, Takafumi Miyasaka, Hiroyuki Murakami, Yusuke Ushijima, Chiharu Takahashi, and Masayoshi Ishii. Climate simulations using MRI-ESM2 with 60 km resolution atmosphere and data assimilated ocean. *J. Meteorol. Soc. Jpn.*, 104:10, 2026. https://doi.org/10.1007/s44394-025-00011-2.

[44] Veronika Eyring, Sandrine Bony, Gerald A Meehl, Catherine A Senior, Bjorn Stevens, Ronald J Stouffer, and Karl E Taylor. Overview of the Coupled Model Intercomparison Project Phase 6 (CMIP6) experimental design and organization. *Geosci. Model Dev.*, 9(5): 1937–1958, 2016. https://doi.org/10.5194/gmd-9-1937-2016.

[45] Nathan P Gillett, Hideo Shiogama, Bernd Funke, Gabriele Hegerl, Reto Knutti, Katja Matthes, Benjamin D Santer, Daithi Stone, and Claudia Tebaldi. The Detection and Attribution Model Intercomparison Project (DAMIP v1.0) contribution to CMIP6. *Geosci. Model Dev.*, 9(10):3685–3697, 2016. https://doi.org/10.5194/gmd-9-3685-2016.

[46] B. C. O'Neill, C. Tebaldi, D. P. van Vuuren, V. Eyring, P. Friedlingstein, G. Hurtt, R. Knutti, E. Kriegler, J.-F. Lamarque, J. Lowe, G. A. Meehl, R. Moss, K. Riahi, and B. M. Sanderson. The Scenario Model Intercomparison Project (ScenarioMIP) for CMIP6. *Geosci. Model Dev.*, 9:3461–3482, 2016. https://doi.org/10.5194/gmd-9-3461-2016.

[47] Masayoshi Ishii, Yoshikazu Fukuda, Shoji Hirahara, Soichiro Yasui, Toru Suzuki, and Kanako Sato. Accuracy of Global Upper Ocean Heat Content Estimation Expected from

Present Observational Data Sets. *SOLA*, 13:163–167, 2017. https://doi.org/10.2151/sola.2017-030.

[48] Shoji Hirahara, Masayoshi Ishii, and Yoshikazu Fukuda. Centennial-Scale Sea Surface Temperature Analysis and Its Uncertainty. *J. Clim.*, 27(1):57–75, 2014. https://doi.org/10.1175/JCLI-D-12-00837.1.

[49] Katarzyna B Tokarska, Martin B Stolpe, Sebastian Sippel, Erich M Fischer, Christopher J Smith, Flavio Lehner, and Reto Knutti. Past warming trend constrains future warming in CMIP6 models. *Science advances*, 6(12):eaaz9549, 2020. https://doi.org/10.1126/sciadv.aaz9549.

[50] Mark D Zelinka, Timothy A Myers, Daniel T McCoy, Stephen Po-Chedley, Peter M Caldwell, Paulo Ceppi, Stephen A Klein, and Karl E Taylor. Causes of Higher Climate Sensitivity in CMIP6 Models. *Geophys. Res. Lett.*, 47(1):e2019GL085782, 2020. https://doi.org/10.1029/2019GL085782.

[51] Valérie Masson-Delmotte, Panmao Zhai, Anna Pirani, Sarah L Connors, Clotilde Péan, Sophie Berger, Nada Caud, Y Chen, L Goldfarb, MI Gomis, et al. Climate Change 2021: the Physical Science Basis. *Working Group I Contribution to the Sixth Assessment Report of the Intergovernmental Panel on Climate Change*, 2(1):2391, 2021. https://doi.org/10.1017/9781009157896.

[52] Norihisa Usui, Tsuyoshi Wakamatsu, Yusuke Tanaka, Nariaki Hirose, Takahiro Toyoda, Shiro Nishikawa, Yosuke Fujii, Yasushi Takatsuki, Hiromichi Igarashi, Haruka Nishikawa, et al. Four-dimensional variational ocean reanalysis: a 30-year high-resolution dataset in the western North Pacific (FORA-WNP30). *J. Oceanogr.*, 73(2):205–233, 2017. https://doi.org/10.1007/s10872-016-0398-5.

[53] Boyin Huang, Peter W Thorne, Viva F Banzon, Tim Boyer, Gennady Chepurin, Jay H Lawrimore, Matthew J Menne, Thomas M Smith, Russell S Vose, and Huai-Min Zhang. Extended Reconstructed Sea Surface Temperature, Version 5 (ERSSTv5): Upgrades, Validations, and Intercomparisons. *J. Clim.*, 30(20):8179–8205, 2017. https://doi.org/10.1175/JCLI-D-16-0836.1.

[54] Na A Rayner, De E Parker, EB Horton, Chris K Folland, Lisa V Alexander, DP Rowell, Elizabeth C Kent, and A Kaplan. Global analyses of sea surface temperature, sea ice, and

night marine air temperature since the late nineteenth century. *J. Geophys. Res. Atmos.*, 108(D14), 2003. https://doi.org/10.1029/2002JD002670.

[55] John J Kennedy, NA Rayner, CP Atkinson, and RE Killick. An Ensemble Data Set of Sea Surface Temperature Change From 1850: The Met Office Hadley Centre HadSST. 4.0.0.0 Data Set. *J. Geophys. Res. Atmos.*, 124(14):7719–7763, 2019. https://doi.org/10.1029/2018JD029867.

[56] Uwe Schulzweida. Cdo User Guide, October 2023. URL https://doi.org/10.5281/zenodo.10020800.

[57] Mark P Baldwin, David B Stephenson, and Ian T Jolliffe. Spatial Weighting and Iterative Projection Methods for EOFs. *J. Clim.*, 22(2):234–243, 2009. https://doi.org/10.1175/2008JCLI2147.1.

[58] K Fujino, EL Lewis, and RG Perkin. The freezing point of seawater at pressures up to 100 bars. *J. Geophys. Res.*, 79(12):1792–1797, 1974. https://doi.org/10.1029/JC079i012p01792.

[59] George L Mellor and Lakshmi Kantha. An ice-ocean coupled model. *J. Geophys. Res. Oceans*, 94(C8):10937–10954, 1989. https://doi.org/10.1029/JC094iC08p10937.

[60] L Shogo Urakawa, Hiroyuki Tsujino, Hideyuki Nakano, Kei Sakamoto, Goro Yamanaka, and Takahiro Toyoda. The sensitivity of a depth-coordinate model to diapycnal mixing induced by practical implementations of the isopycnal tracer diffusion scheme. *Ocean Model.*, 154: 101693, 2020. https://doi.org/10.1016/j.ocemod.2020.101693.

[61] Yukio Kurihara, Toshiyuki Sakurai, and Turane Kuragano. Global daily sea surface temperature analysis using data from satellite microwave radiometer, satellite infrared radiometer and in-situ observations (in japanese). *Weather Bull.*, 73:S1–S18, 2006.

[62] Hyodae Seo, Young-Oh Kwon, and Jong-Jin Park. On the effect of the East/Japan Sea SST variability on the North Pacific atmospheric circulation in a regional climate model. *J. Geophys. Res. Atmos.*, 119(2):418–444, 2014. https://doi.org/10.1002/2013JD020523.

[63] Hiroshi G Takahashi, Noriko N Ishizaki, Hiroaki Kawase, Masayuki Hara, Takao Yoshikane, Xieyao Ma, and Fujio Kimura. Potential Impact of Sea Surface Temperature on Winter

Precipitation over the Japan Sea Side of Japan: A Regional Climate Modeling Study. *J. Meteorol. Soc. Jpn.*, 91(4):471–488, 2013. https://doi.org/10.2151/jmsj.2013-404.

[64] Masaya Nosaka, Hiroaki Kawase, Hidetaka Sasaki, and Akihiko Murata. Influence of the Temporal Resolution of Sea Surface Temperature on Winter Precipitation over the Coastal Area of the Sea of Japan. *SOLA*, 15:107–112, 2019. https://doi.org/10.2151/sola.2019-020.

[65] Yusuke Ushijima, Hiroyuki Tsujino, Ryo Mizuta, Hideyuki Nakano, Hirokazu Endo, Hideo Shiogama, Yukiko Imada, Osamu Arakawa, Seiji Yukimoto, Yuma Kawakami, L. Shogo Urakawa, Takahiro Toyoda, and Masayoshi Ishii. Bias-corrected Ocean Temperature, Salinity, and Sea-Ice Concentration Datasets for Present, Non-Warming, and Future Climates [dataset], 2026. https://doi.org/10.5281/zenodo.20825753.

[66] Changlin Chen and Guihua Wang. Role of North Pacific Mixed Layer in the Response of SST Annual Cycle to Global Warming. *J. Clim.*, 28(23):9451–9458, 2015. https://doi.org/10.1175/JCLI-D-14-00349.1.

[67] Hai Wang and Yu-Jun Wen. Climate response to the spatial and temporal evolutions of anthropogenic aerosol forcing. *Clim. Dyn.*, 59(5):1579–1595, 2022. https://doi.org/10.1007/s00382-021-06059-2.

[68] Tomoki Iwakiri and Masahiro Watanabe. Mechanisms linking multi-year La Niña with preceding strong El Niño. *Sci. Rep.*, 11(1):17465, 2021. https://doi.org/10.1038/s41598-021-96056-6.

[69] Daohua Bi, Martin Dix, Simon Marsland, Siobhan O'farrell, Arnold Sullivan, Roger Bodman, Rachel Law, Ian Harman, Jhan Srbinovsky, Harun A Rashid, et al. Configuration and spin-up of ACCESS-CM2, the new generation Australian Community Climate and Earth System Simulator Coupled Model. *J. South. Hemisph. Earth Syst. Sci.*, 70(1):225–251, 2020. https://doi.org/10.1071/ES19040.

[70] Gokhan Danabasoglu, J-F Lamarque, J Bacmeister, DA Bailey, AK DuVivier, Jim Edwards, LK Emmons, John Fasullo, R Garcia, Andrew Gettelman, et al. The Community Earth System Model version 2 (CESM2). *J. Adv. Model. Earth Syst.*, 12(2):e2019MS001916, 2020. https://doi.org/10.1029/2019MS001916.

[71] Aurore Voldoire, David Saint-Martin, Stéphane Sénési, B Decharme, A Alias, Matthieu Chevallier, Jeanne Colin, J-F Guérémy, Martine Michou, M-P Moine, et al. Evaluation of CMIP6 DECK Experiments With CNRM-CM6-1. *J. Adv. Model. Earth Syst.*, 11(7): 2177–2213, 2019. https://doi.org/10.1029/2019MS001683.

[72] Neil C Swart, Jason NS Cole, Viatcheslav V Kharin, Mike Lazare, John F Scinocca, Nathan P Gillett, James Anstey, Vivek Arora, James R Christian, Sarah Hanna, et al. The Canadian Earth System Model version 5 (CanESM5. 0.3). *Geosci. Model Dev.*, 12(11): 4823–4873, 2019. https://doi.org/10.5194/gmd-12-4823-2019.

[73] Olivier Boucher, Jérôme Servonnat, Anna Lea Albright, Olivier Aumont, Yves Balkanski, Vladislav Bastrikov, Slimane Bekki, Rémy Bonnet, Sandrine Bony, Laurent Bopp, et al. Presentation and Evaluation of the IPSL-CM6A-LR Climate Model. *J. Adv. Model. Earth Syst.*, 12(7):e2019MS002010, 2020. https://doi.org/10.1029/2019MS002010.

[74] Hiroaki Tatebe, Tomoo Ogura, Tomoko Nitta, Yoshiki Komuro, Koji Ogochi, Toshihiko Takemura, Kengo Sudo, Miho Sekiguchi, Manabu Abe, Fuyuki Saito, et al. Description and basic evaluation of simulated mean state, internal variability, and climate sensitivity in MIROC6. *Geosci. Model Dev.*, 12(7):2727–2765, 2019. https://doi.org/10.5194/gmd-12-2727-2019.

[75] Thorsten Mauritsen, Jürgen Bader, Tobias Becker, Jörg Behrens, Matthias Bittner, Renate Brokopf, Victor Brovkin, Martin Claussen, Traute Crueger, Monika Esch, et al. Developments in the MPI-M Earth System Model version 1.2 (MPI-ESM1.2) and Its Response to Increasing CO2. *J. Adv. Model. Earth Syst.*, 11(4):998–1038, 2019. https://doi.org/10.1029/2018MS001400.

[76] Seiji Yukimoto, Hideaki Kawai, Tsuyoshi Koshiro, Naga Oshima, Kohei Yoshida, Shogo Urakawa, Hiroyuki Tsujino, Makoto Deushi, Taichu Tanaka, Masahiro Hosaka, et al. The Meteorological Research Institute Earth System Model Version 2.0, MRI-ESM2.0: Description and Basic Evaluation of the Physical Component. *J. Meteorol. Soc. Jpn.*, 97(5): 931–965, 2019. https://doi.org/10.2151/jmsj.2019-051.

[77] Alistair A Sellar, Colin G Jones, Jane P Mulcahy, Yongming Tang, Andrew Yool, Andy Wiltshire, Fiona M O'connor, Marc Stringer, Richard Hill, Julien Palmieri, et al. UKESM1:

925 Description and Evaluation of the U.K. Earth System Model. *J. Adv. Model. Earth Syst.*,
926 11(12):4513–4558, 2019. https://doi.org/10.1029/2019MS001739.